EXTENDED SUBMILLIMETER EMISSION OF THE GALACTIC CENTER AND NEAR-INFRARED/SUBMILLIMETER VARIABILITY OF ITS SUPERMASSIVE BLACK HOLE

The Astrophysical Journal, 738:158 (19pp), 2011 September 10 doi:10.1088/0004-637X/738/2/158

EXTENDED SUBMILLIMETER EMISSION OF THE GALACTIC CENTER AND NEAR-INFRARED/SUBMILLIMETER VARIABILITY OF ITS SUPERMASSIVE BLACK HOLE*

M. García-Marín[1], A. Eckart[1,2], A. Weiss[2], G. Witzel[1], M. Bremer[1], M. Zamaninasab[2,1], M. R. Morris[3], R. Schödel[4], D. Kunneriath[1,16], S. Nishiyama[5,17], F. Baganoff[6], M. Dovčiak[7], N. Sabha[1], W. J. Duschl[8,9], J. Moultaka[10], V. Karas[6], F. Najarro[11], K. Mužić[15], C. Straubmeier[1], S. N. Vogel[12], M. Krips[13], and H. Wiesemeyer[13]
[1] I. Physikalisches Institut, Universität zu Köln, Zülpicher Str. 77, 50937 Köln, Germany; maca@ph1.uni-koeln.de
[2] Max-Planck-Institut für Radioastronomie, Auf dem Hügel 69, 53121 Bonn, Germany
[3] Department of Physics and Astronomy, University of California, Los Angeles, CA 90095-1547, USA
[4] Instituto de Astrofísica de Andalucía, Camino Bajo del Huétor 50, 18008 Granada, Spain
[5] Department of Astronomy, Kyoto University, Kyoto 6006-8502, Japan
[6] Center for Space Research, Massachusetts Institute of Technology, Cambridge, MA 02139-4307, USA
[7] Astronomical Institute, Academy of Sciences, Boční II, 14131 Prague, Czech Republic
[8] Instituts für Theoretische Physic und Astrophysik, Christian-Albrechts-Universität zu Kiel, Leibnizstr. 15, 24118 Kiel, Germany
[9] Steward Observatory, The University of Arizona, 933 North Cherry Avenue, Tucson, AZ 85721, USA
[10] LATT, Université de Toulouse, CNRS, 14 avenue Édouard Belin, 31400 Toulouse, France
[11] Centro de Astrobiología (CSIC/INTA), Ctra de Torrejón a Ajalvir, km 4, 28850 Torrejón de Ardoz, Madrid, Spain
[12] Department of Astronomy, University of Maryland, College Park, MD 20742-2421, USA
[13] Institut de Radio Astronomie Millimetrique, Domaine Universitaire, 38406 Saint-Martin d'Hères, France
[14] IRAM, Avenida Divina Pastora, 7 Núcleo Central, 18012 Granada, Spain
[15] Department of Astronomy & Astrophysics, University of Toronto, 50 St. George Street, Toronto, ON M55 3H4, Canada
Received 2010 February 27; accepted 2011 May 24; published 2011 August 22

ABSTRACT

The innermost tens of parsecs of our Galaxy are characterized by the presence of molecular cloud complexes surrounding Sgr A*, the radiative counterpart of the supermassive black hole ($\sim 4 \times 10^6\ M_\odot$) at the Galactic center. We seek to distinguish the different physical mechanisms that dominate the molecular clouds at the Galactic center, with special emphasis on the circumnuclear disk (CND). We also want to study the energy flow and model the variable emission of Sgr A*. Our study is based on NIR and submillimeter (sub-mm) observations. Using sub-mm maps, we describe the complex morphology of the molecular clouds and the circumnuclear disk, along with their masses (of order 10^5–$10^6\ M_\odot$), and derive also the temperature and spectral index maps of the regions under study. We conclude that the average temperature of the dust is 14 ± 4 K. The spectral index map shows that the 20 and 50 km s^{-1} clouds are dominated by dust emission. Comparatively, in the CND and its surroundings the spectral indices decrease toward Sgr A* and range between about 1 and -0.6. These values are mostly explained with a combination of dust, synchrotron, and free–free emission in different ratios. The presence of non-thermal emission also accounts for the apparent low temperatures derived in these areas, indicating their unreliability. The Sgr A* light curves show significant flux density excursions in both the NIR and sub-mm domains. We have defined a classification system to account for the NIR variability of Sgr A*. Also, we have modeled on the NIR/sub-mm events. From our modeling results we can infer a sub-mm emission delay with respect to the NIR; we argue that the delay is due to the adiabatic expansion of the synchrotron source components.

Key words: Galaxy: center – Galaxy: nucleus – infrared: general – submillimeter: general

Online-only material: color figures

1. INTRODUCTION

The Galactic center (GC) offers the unique opportunity of studying the central region of a galaxy at a resolution not achievable in any other extragalactic source. The inner parsecs of the GC have been extensively mapped in submillimeter (sub-mm) continuum (e.g., Mezger et al. 1989; Dent et al. 1993; Lis & Carlstrom 1994; Pierce-Price et al. 2000), radio continuum (e.g., Ekers et al. 1983; Yusef-Zadeh et al. 1986, 2004; Anantharamaiah et al. 1991; Davidson et al. 1992, and references therein), molecular transitions (e.g., Harris et al. 1985; Guesten et al. 1987; Jackson et al. 1996; Wright et al. 2001; Herrnstein & Ho 2002, 2005), and infrared (e.g., Genzel et al. 1984; Gatley et al. 1986; Latvakoski et al. 1999, among others). All these studies have demonstrated the complexity of the system of molecular clouds around the GC and have tried to explain their relative unprojected distribution. Also, radio studies have revealed a variety of thermal and non-thermal structures (e.g., Yusef-Zadeh & Morris 1987a, 1987b, 1987c). In the sub-mm domain, Pierce-Price et al. (2000) derived a spectral indices map of the central molecular zone (CMZ), along with a general temperature analysis. However, the detailed temperature and spectral indices distribution of the inner tens of parsecs were not discussed. In the radio continuum, the most important structure of the central parsecs of the Milky Way is the Sagittarius A complex (Sgr A). At high spatial resolution this complex breaks into two very specific components: Sgr A East, a non-thermal shell which has been supposedly created by a supernovae explosion (Maeda et al. 2002), and Sgr A West, a region dominated by thermal radiation. Sgr A West consists of a collection of streamers (the so-called

* Based on observations made with ESO APEX and VLT telescopes under programme 081.B-0648(B). Based also on SCUBA/JCMT archive data, project M98AU64.
[16] Now at Astronomical Institute, Academy of Sciences, Boční II, 14131 Prague, Czech Republic.
[17] Research Fellow of the Japan Society for the Promotion of Science (JSPS).

Table 1
Observations Log

Telescope	Instrument	Wavelength (μm)[a]	Start Time (UT)	Stop Time (UT)
APEX	LABOCA	870	2008 May 27 07:02:53	2008 May 27 10:39:52
APEX	LABOCA	870	2008 May 28 07:06:35	2008 May 28 10:46:39
APEX	LABOCA	870	2008 May 29 06:58:15	2008 May 29 10:54:58
APEX	LABOCA	870	2008 May 30 08:18:20	2008 May 30 09:26:41
APEX	LABOCA	870	2008 Jun 3 04:56:55	2008 Jun 3 10:22:55
VLT UT 4	NACO	2.2	2008 May 25 04:55:46	2008 May 25 05:24:23
			06:05:20	10:35:39
VLT UT 4	NACO	2.2	2008 May 26 04:53:26	2008 May 26 05:21:58
VLT UT 4	NACO	2.2	2008 May 27 04:52:05	2008 May 27 08:30:42
VLT UT 4	NACO	2.2	2008 May 28 08:37:28	2008 May 28 09:39:44
VLT UT 4	NACO	2.2	2008 May 30 05:44:27	2008 May 30 06:13:12
			08:24:33	09:45:26
VLT UT 4	NACO	2.2	2008 May 31 05:14:10	2008 May 31 05:42:45
VLT UT 4	NACO	2.2	2008 Jun 1 05:02:24	2008 Jun 1 05:31:01
			06:04:52	10:53:14
VLT UT 4	NACO	2.2	2008 Jun 3 08:37:23	2008 Jun 3 09:58:59
VLT UT 4	NACO	3.8	2008 May 26 05:42:55	2008 May 26 10:36:41
VLT UT 4	NACO	3.8	2008 May 27 08:39:60	2008 May 27 10:19:57
VLT UT 4	NACO	3.8	2008 May 28 08:22:51	2008 May 28 08:28:31
VLT UT 4	NACO	3.8	2008 May 30 06:40:44	2008 May 30 08:10:49
			09:57:42	10:41:27
VLT UT 4	NACO	3.8	2008 May 31 06:09:17	2008 May 31 10:29:36
VLT UT 4	NACO	3.8	2008 Jun 2 05:00:54	2008 Jun 2 05:15:12
			05:48:29	10:14:42
VLT UT 4	NACO	3.8	2008 Jun 3 04:41:34	2008 Jun 3 08:20:14
Subaru	CIAO	2.2	2008 May 27 10:50:09	2008 May 27 12:37:05
Subaru	CIAO	2.2	2008 May 28 10:23:48	2008 May 28 13:35:32
Subaru	CIAO	2.2	2008 May 29 09:22:51	2008 May 29 12:57:06

Note. [a] Central wavelength of the filter used.

mini-spiral) which are surrounded by the circumnuclear disk (CND). The CND is formed by a continuous clumpy ring with two prominent concentrations forming a lobed structure which has been detected at several wavelengths. In the middle of the CND, at the very center of the Milky Way, we find the non-thermal source Sgr A*, where stellar orbit studies have proven the existence of a supermassive black hole (SMBH).

Sgr A* is a strongly variable source whose variability has been studied at all wavelengths from radio to TeV energies, showing that the changes occur on timescales from hours to years (e.g., Zhao et al. 2001; Mauerhan et al. 2005; Eckart et al. 2006a; Yusef-Zadeh et al. 2008, 2009; Marrone et al. 2008). Several flares have provided evidence of decaying millimeter and submillimeter emission following simultaneous NIR/X-ray flares. Much effort has been invested in studying the variability of Sgr A*, but until now limited simultaneous NIR/sub-mm studies have been carried out (e.g., Eckart et al. 2006b, 2008b; Yusef-Zadeh et al. 2006, 2009; Marrone et al. 2008).

In this paper we present the results from our Atacama Pathfinder Experiment (APEX)/Very Large Telescope (VLT) 2008 coordinated campaign, with complementary Subaru and James Clerk Maxwell Telescope (JCMT) data. We especially want to take the maximum advantage of our APEX sub-mm data, and to give a complete sub-mm view of the GC. Hence, the paper deals with two main topics: first the extended emission of the central tens of parsecs of the galaxy and the different mechanisms responsible for it. This analysis is based on the APEX and JCMT sub-mm archive maps. Second, the intrinsic variability of Sgr A* and the physical process behind it. This part implies the analysis and modeling of a set of light curves in both sub-mm and NIR. Section 2 details the observations, and Section 3 is dedicated to the analysis of the data. In Section 4 and Section 5, we discuss the 870 μm GC extended emission, and the masses of the most important molecular clouds and the CND. Section 6 deals with the temperature and spectral index distribution. Section 7 presents the general characteristics of the light curves and presents our NIR light-curve classification, whereas Section 8 deals with the light curves analysis and modeling. Finally, Section 9 summarizes the most important results of the paper.

The assumed mass of and distance to Sgr A* are $4.4 \times 10^6\ M_\odot$ (Eckart & Genzel 1996, 1997; Eckart et al. 2002; Schödel et al. 2002; Eisenhauer et al. 2003; Ghez et al. 2000, 2005, 2008; Gillessen et al. 2009) and 8.3 kpc (Reid 1993), consistent with recent results from Eisenhauer et al. (2003), Ghez et al. (2005), Ghez et al. (2008), and Lu et al. (2009).

2. OBSERVATIONS

2.1. The APEX/LABOCA Sub-mm On-the-fly Maps

We obtained sub-mm (870 μm) on-the-fly (OTF) maps of the GC region using the Large APEX Bolometer Camera (LABOCA; Siringo et al. 2009) on the APEX telescope, Chile. The observations were carried out during five nights between 2008 May 27 and June 3 (see observing log details in Table 1), as part of our ground-based, multi-wavelength monitoring program. LABOCA covers a total bandwidth of 60 GHz in the 345 GHz atmospheric window, and is characterized by a beam size (FWHM of the point-spread function (PSF)) of 19″ at 870 μm. From this APEX campaign, the data corresponding to 2008 June 3 have already been published in Eckart et al. (2008b).

During each observing night we took a series of OTF maps of the GC innermost parsecs, interleaved with observations of G10.62 or IRAS16293-2422 as secondary calibrators. For the GC maps we used an integration time of 280 s, a scanning speed of $3'\ s^{-1}$, and a mapping step of $30''$. We also systematically changed the observation angle (orthogonal to the galactic plane) by -10°, 0°, and 10°, to avoid spurious artifacts. In this way we end up with $0.^\circ5 \times 0.^\circ8$ GC maps with an rms noise level of 150 mJy beam^{-1}. For full details of the observation technique, the reader is referred to Eckart et al. (2008b).

2.2. The JCMT/SCUBA Sub-mm Archive Maps

Complementary sub-mm 450 and 850 μm archive maps (project m98au64) have also been used. These maps were obtained with the Submillimeter Common-User Bolometer Array (SCUBA; Holland et al. 1999), a continuum array receiver located at the 15 m JCMT in Mauna Kea, Hawaii. They are a subset of the GC survey shown by Pierce-Price et al. (2000). With a field of view of 2.3 arcmin in diameter, SCUBA is formed by two hexagonal arrays of bolometric detectors called Long Wave (LW; 850 μm, 31 pixels) and Short Wave (SW; 450 μm, 91 pixels). Using a dichroic beamsplitter, SCUBA is capable of simultaneously using both arrays. The diffraction-limited resolution corresponds to about $7.''5$ at 450 μm, and $14''$ at 850 μm.

The observing mode used was scan-mapping, in which the telescope scans the array across the sky while chopping the secondary mirror to produce a differential map of the source. For SCUBA it is recommended to use six different chop configurations: chop throws of $20''$, $30''$, and $65''$ each with chop position angles of 0 deg (Decl. chopping) and 90 deg (R.A. chopping) in a coordinate frame fixed on the sky. For the present case a scan velocity of $24''s^{-1}$ was used.

2.3. The VLT/NACO NIR Data

Our NIR adaptive optics (AO) data were obtained between 2008 May 25 and June 3 with NACO (Lenzen et al. 2003; Rousset et al. 2003) at the 8 m ESO VLT unit telescope 4 (YEPUN) in Paranal, Chile (see Table 1). Some of these VLT data have already been published. Specifically, the 2008 May 26 and June 3 light curves have been published in Kunneriath et al. (2010) and Eckart et al. (2008b), respectively. Details of the observations are given in Table 2. From that table it is straightforward to calculate the total integration time as DIT × NDIT × N. The seeing given is that obtained at visible wavelengths in Paranal. The stability of the atmospheric conditions provided good AO corrections all over the run.

We used the dithering technique to produce a mosaic of about $20'' \times 20''$. Interleaved off-source observations of a dark cloud ($60''$E and $60''$N of Sgr A*) were used to measure the rapid NIR L'-band background variability. The K-band sky background was estimated as the median of several dithered observations of another dark cloud ($713''$W and $400''$N of Sgr A*). See Eckart et al. (2008b) for more details of the observations.

2.4. The Subaru/CIAO NIR Data

We present additional NIR Ks-band observations obtained by Nishiyama et al. (2009a) at the Subaru telescope (Iye et al. 2004), using the CIAO coronographic imager (Tamura et al. 2003) and the AO36 adaptive optics system (Takami et al. 2004). From this Subaru observing campaign the data from 2009 May 29 were first published by Nishiyama et al. (2009b), and subsequently by Zamaninasab et al. (2010).

Table 2
NACO/NIR Observation Details

λ[a]	DIT[b]	NDIT[c]	N[d]	Pixel Scale[e]	Seeing[f]
2.2 μm	10 s	4	80	$0.''027$	$\sim 1.''0$–$1.''4$
3.8 μm	0.2 s	150	150	$0.''027$	$\sim 1.''0$–$1.''4$

Notes.
[a] Filter central wavelength.
[b] Detector integration time in seconds.
[c] Number of averaged exposures of integration time DIT.
[d] N is the number of images.

Details of the observations are given in Table 1. The image provided by CIAO covers $22.''2 \times 22.''2$ of the sky. Sky measurements of a dark cloud located a few arcmin northwest from Sgr A* were interleaved with the Sgr A* observations. More details about these observations can be found in Nishiyama et al. (2009a).

3. DATA ANALYSIS

3.1. LABOCA 870 μm Map Data Reduction and Light-curve Derivation

The data reduction of the LABOCA data is described in detail in Eckart et al. (2008b). Briefly, we used the BoA[18] software package to perform a standard data reduction, including opacity ($\tau \sim 0.3$ up to 0.7 toward the GC direction) and flat-field corrections, and correlated sky and instrumental noise removal. This data reduction has been optimized for constraining the Sgr A* flux; hence, the filtering applied may partially affect the extended emission and some flux may be lost in the process. Once the initial data reduction was finished, our main objective was to derive the Sgr A* light curves. To do that, on each individual scan we model Sgr A* as a point-source emitter using a Gaussian fitting and calculating its peak. The modeling process involves the prior removal of the extended sub-mm emission, obtained by co-adding all individual maps (corrected for pointing offsets) and afterward subtracting the resultant averaged central point source. Apart from allowing us to precisely derive the Sgr A* flux, the co-addition of individual maps also provided us with a high signal-to-noise ratio (S/N), $48' \times 25'$, fully sampled map of the sub-mm emission in the GC region (see Figure 1). By subtracting the extended emission we make sure that the background emission is removed, and we are able to better isolate the contribution coming from Sgr A*. The main uncertainty of this process is the subtraction of the point source, which will result in a small intensity offset of the light curve. By testing several models and repeating the data reduction we estimate that, using a model that removes the source without oversubtraction, this effect is less than 10% of the peak flux density of Sgr A*. To calibrate the data we used τ (values based on sky dip and radiometer measurements), secondary calibrators, and compared with the reference map. The flux variation on the secondary calibrators at different epochs is about 10%. However, we estimate the error to be of the order of 4%, which is the relative point-to-point uncertainty in the light-curve calibration. The resulting light curves are shown in Figure 2.

[18] BoA (Bolometer Array Analysis Software): http://astro.uni-bonn.de/boawiki/boa.

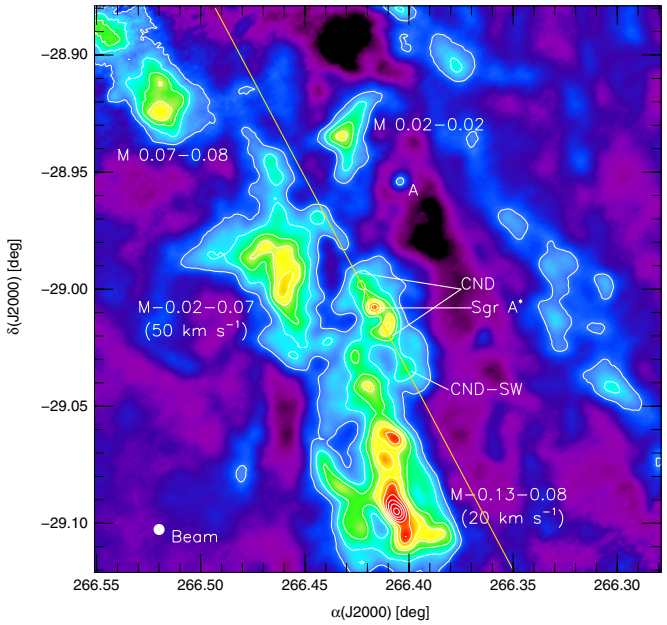

Figure 1. LABOCA 870 μm map of the GC, showing the complex extended thermal emission surrounding Sgr A*. The most important molecular clouds and the CND are labeled, along with the position of Sgr A*. The region marked with an A is the one used for cross-checking the point-to-point flux uncertainties. Contour levels indicate 2, 3, 4, 5, 6, 7, 8, 9, and 10 Jy beam^{-1}. The approximate location of the galactic plane is indicated by the yellow line. North is up, east to the left.

(A color version of this figure is available in the online journal.)

To further check the significance of the Sgr A* variability, we conducted independent flux measurements of a point-like source observed toward the southwest of the molecular cloud M 0.02-0.02 (labeled A in Figure 1). The uncertainties derived are 8%, 10%, 12%, 5%, and 6% for May 27, 28, 29, 30, and June 3, respectively. The variations in the individual flux values are higher than the 4% uncertainty derived from the different reference sources. This overestimation of the uncertainty is most likely due to the low S/N of this source, rather than to uncompensated opacity variations or pointing issues. However, even considering these uncertainties, the variability of Sgr A* is still significant, therefore validating our method.

3.2. SCUBA Sub-mm Data Reduction

The JCMT data have been retrieved fully reduced from the archive. This section gives a summary of the online data reduction procedure. The data were reduced with the SCUBA User Reduction Facility (SURF; Jenness & Lightfoot 1998), which uses the *Emmerson 2* deconvolution algorithm to combine the multiple chop throw images of the map field. The data reduction includes flat-fielding the array, correcting for atmospheric extinction, despiking, and generating a rectangularly sampled image. The regridded image can be in any pixel size, and the beam sizes were taken into account: approximately 7 arcsec at 450 μm and 14 arcsec at 850 μm. The online system regrids with 3″pixel^{-1}. The calibrated maps retrieved are shown in Figure 3. The estimated rms is 0.7 and 0.2 Jy beam^{-1} for the 450 and 850 μm maps, respectively. The total size of the derived maps is about 13′ × 13′.

3.3. VLT NIR Data Reduction and Photometry

The NIR data reduction involves flat-fielding, sky subtraction, correction for dead or bad pixels, and sky-background subtraction. There are two main challenges that have to be faced when analyzing the NIR emission coming from Sgr A*. The first is that it is located in a very crowded field, and the second is its intrinsic weakness when it is not in a flaring state. To deal with these, after the basic data reduction was finished, PSFs were subtracted from the images using *Starfinder* (Diolaiti et al. 2000). Subsequently, we deconvolved the images using the Lucy–Richardson (LR) algorithm (Lucy 1974; Richardson 1972), and restored the beam using a Gaussian beam whose FWHM was the nominal resolution at the correspondent wavelength. We finally obtain a resolution of about 60 and 104 mas at 2.2 and 3.8 μm, respectively.

We used circular aperture photometry (52 mas radius) to estimate the flux density of the individual sources, and $A_K = 2.8$ and $A_{L'} = 1.8$ to correct for extinction. The K- and L'-band flux densities of IRS16SW, IRS16C, IRS16NE, and IRS21 (R. Schödel 2009, private communication) were used to perform the relative flux calibration.

We used the (known) fluxes and positions of 14 sources within 1.″6 from Sgr A* to carry out its relative photometry, and derived the uncertainties using the reference stars S2 and S10. Finally, the background in the immediate vicinity of Sgr A* was measured, and subsequently corrected, in a close region where no apparent flux was measured. Figures 2 and 4 show the background-subtracted light curves obtained.

3.4. Subaru Ks-band Data Reduction and Photometry

The NIR Subaru data reduction included dark- and flat-field correction, sky-background estimation and subtraction, and bad pixel correction (Nishiyama et al. 2009a). All these steps were performed using the Image Reduction and Analysis Facility (IRAF)[19]. Once the images were reduced, the program *Starfinder* (Diolaiti et al. 2000) was used to extract a PSF via point-source fitting from each image. Each image was afterward deconvolved using the LR algorithm (Lucy 1974; Richardson 1972). The light curves obtained are shown in Figure 2.

4. GENERAL CHARACTERISTICS OF THE 870 μm SUBMILLIMETER EXTENDED EMISSION STRUCTURE

The 870 μm LABOCA continuum map (see Figure 1) shows approximately the innermost 37 × 34 pc^2 of the GC (assuming a distance of 8.0 kpc, which corresponds to a scale of 2.3 pc arcmin^{-1}). Its main structures run parallel to the galactic plane, and they are in good agreement with previous sub-mm surveys of the region, including at 800 and 450 μm (Dent et al. 1993), at 800 μm (Lis & Carlstrom 1994), and at 850 and 450 μm (Pierce-Price et al. 2000). These sub-mm continuum structures trace the temperature-weighted column density of dust. However, the same molecular clouds and the CND have also been detected in molecular lines (e.g., Guesten et al. 1981; Okumura et al. 1991; Oka et al. 1996; Tsuboi et al. 1999). Based on CO and CS data, Zylka et al. (1990) concluded that the Sgr A complex is formed by up to five distinct clouds partially overlapping in space as well as in velocity. For a more recent work on the line-of-sight placement of the GC molecular clouds, see Herrnstein (2003).

In our 870 μm map, the CND is observed as an elliptically-shaped structure. Consistent with observations at other wavelengths, it presents two bright lobes (see Figures 1 and 5, left),

[19] IRAF is distributed by the National Optical Astronomy Observatory (NOAO), which is operated by the Association of Universities for Research in Astronomy (AURA), Inc., under cooperative agreement with the National Science Foundation.

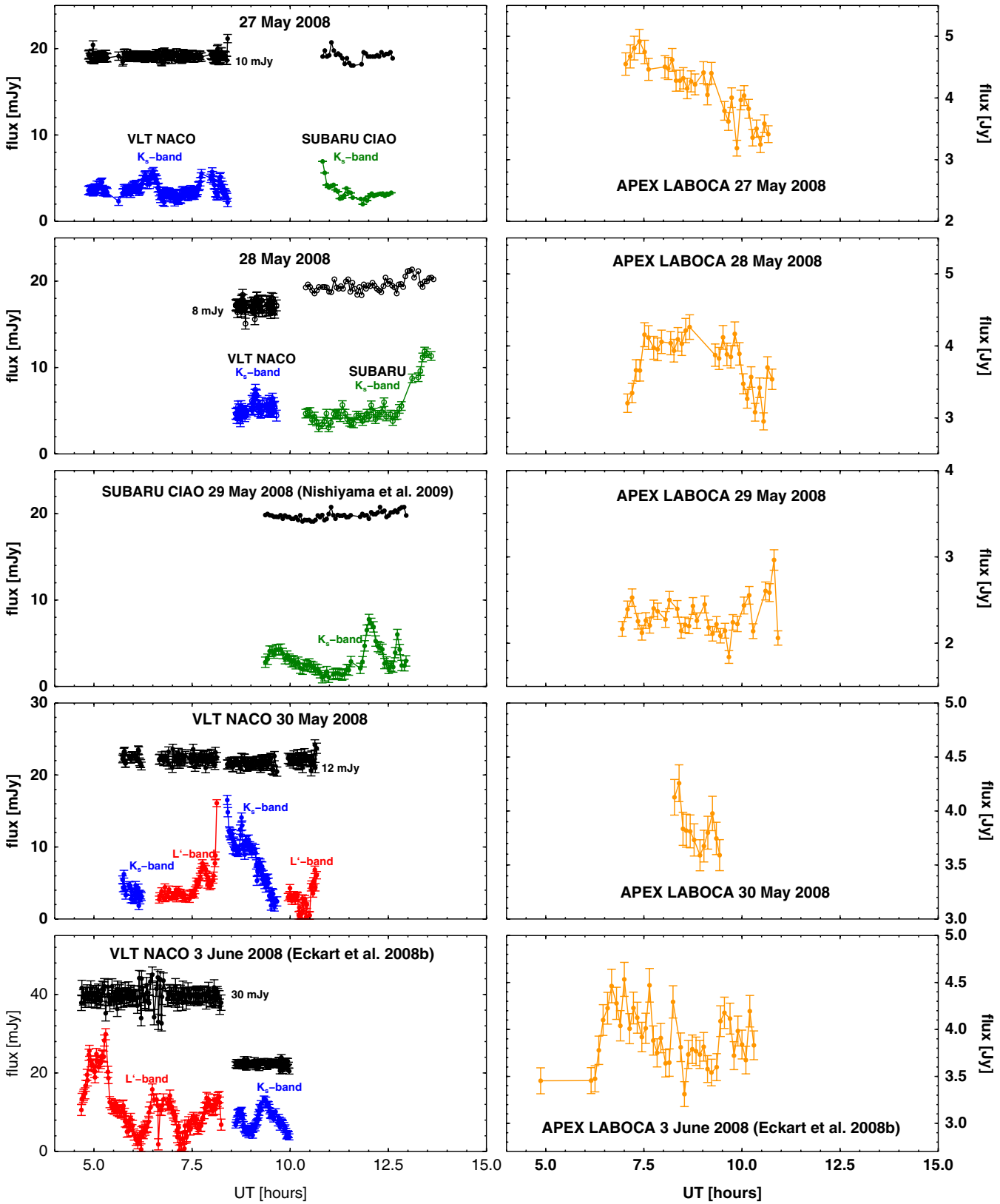

Figure 2. Sgr A* coordinated NIR and sub-mm light curves for 2008 May–June. References for previously published flares are indicated. Left column: NACO/VLT and CIAO/Subaru NIR light curves. Blue and red represent NACO *Ks* and L' bands, respectively, whereas the *Ks*-band CIAO/Subaru light curves are shown in green. The corresponding calibration stars are shown in black. The number next to the VLT calibration stars represents an offset that has been added for representation purposes. For a proper comparison with the *Ks* band, we have scaled Sgr A* L'-band data by a factor 0.72, which corresponds to a spectral index of −0.6 (Hornstein et al. 2007). Right column: LABOCA/APEX light curves.

(A color version of this figure is available in the online journal.)

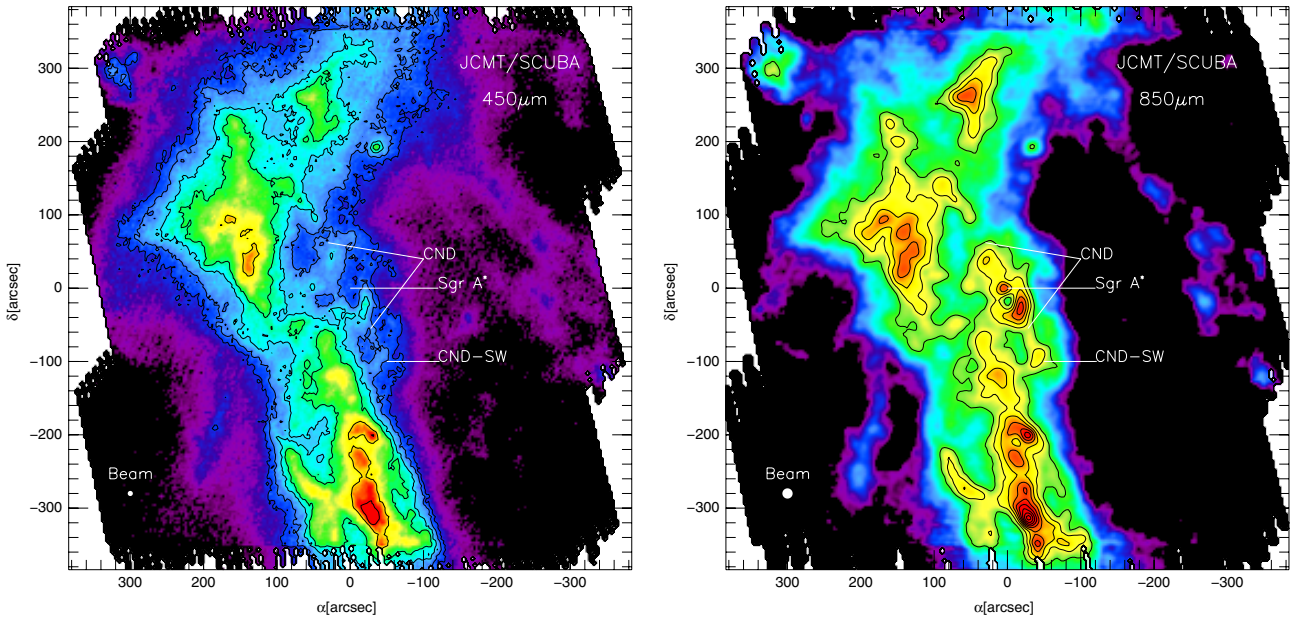

Figure 3. JCMT SCUBA archive maps. North is up, east to the left. Left: 450 μm map. Contours represent 2, 5, 10, 15, 30, and 45 Jy beam^{-1}. Right: 850 μm map. Contours represent 2, 3, 4, 5, 6, 7, 8, 9, and 10 Jy beam^{-1}.

(A color version of this figure is available in the online journal.)

with the intensity peak of the one toward the southwest being about 1.7 times stronger than the one to the northeast. The presence of these lobes is generally interpreted as being due to limb brightening of the torus (e.g., Gatley et al. 1986; Burton & Allen 1992; Yusef-Zadeh et al. 2001). At about 4.0 pc from Sgr A*, and aligned with the apparent major axes of the CND, the bright condensation labeled CND-SW (Figure 1) may be connected with the CND itself.

The 870 μm continuum emission peaks in a region located at a projected distance of about 12 pc from Sgr A*, in the molecular cloud M-0.13-0.08, also known as the 20 km s^{-1} cloud. In projection, its conical shape points toward (and connects with) the CND structure. Aside from the previously mentioned continuum works, the 20 km s^{-1} cloud has also been detected in ammonia (Guesten et al. 1981; Okumura et al. 1991).

To the east of Sgr A* we find M-0.02-0.07, also known as the 50 km s^{-1} cloud. Its structure is irregular, and in projection it does not have a clear connection with the CND. The cloud M 0.07-0.08 belongs to a larger elongated complex which runs almost parallel to the galactic plane, with its long axis pointing to Sgr A*. Finally, to the northeast of Sgr A* we find M 0.02-0.02. This irregularly shaped cloud is the smallest one and represents the fourth most relevant of the inner 37 × 34 pc^2.

5. 870 μm-BASED MASS DISTRIBUTION

The 870 μm continuum map can also be used to calculate the total CND and cloud masses from their integrated fluxes. In this case, the filtered flux mentioned in Section 3.1 is a source of error, which may lead to an underestimation of the extended emission contribution, and therefore the mass estimation. Considering this, the calculations given here should be treated as a lower limit to the mass of the molecular clouds and the CND.

Assuming that the dust emission is optically thin in the sub-mm continuum, the total mass of the most important clouds and the CND can be derived using the expression (Hildebrand 1983)

$$M = \frac{d^2 F_\nu R}{B_\nu(T_{\rm dust})\kappa_\nu}, \quad (1)$$

where d is the distance to the source, F_ν is the measured flux density, R is the gas-to-dust ratio, $B_\nu(T_{\rm dust})$ is the Planck function for the assumed dust temperature, and κ_ν is the dust opacity. The dust opacity is given by

$$\kappa_\nu = \kappa_0(\nu/1.2 \times 10^{12}\ {\rm Hz})^\beta, \quad (2)$$

where $\kappa_0 = 0.1$ cm^2 g^{-1} and β is the dust emissivity. Following Lis et al. (1991) we have adopted a uniform dust temperature of 30 K, higher than the 20 K derived by Pierce-Price et al. (2000). We have assumed the dust emissivity to be 2.0 (the theoretical maximum for crystalline dust grains; see Pierce-Price et al. 2000) and the gas-to-dust ratio to be 100.

We have defined the CND flux as that limited by the 2 Jy beam^{-1} contour (see Figure 1). This limit constrains well the ring and the two lobes. For the molecular clouds, we have integrated approximately the area limited by the 1 Jy beam^{-1}. Using this, the integrated fluxes for the CND and the most important molecular clouds range between about 35 and 320 Jy, whereas the total masses are all of the order of 10^5–10^6 $M_\odot$ (see specific values in Table 3). The errors in the masses have been derived varying the β value by 20%, as the mass is more sensitive

Table 3
Integrated Fluxes and Masses Based on the LABOCA Map

Region	Flux (Jy)	Mass ($\times 10^5$ $M_\odot$)
CND	55 ± 4	7.9 ± 3.1
M-0.13-0.08 (20 km s^{-1})	323 ± 32	46.5 ± 18.2
M-0.02-0.07 (50 km s^{-1})	205 ± 18	29.5 ± 11.6
M 0.07-0.08	114 ± 8	16.0 ± 6.4
M 0.02-0.02	35 ± 5	5.0 ± 1.9

Note. The assumed temperature is 30 K.

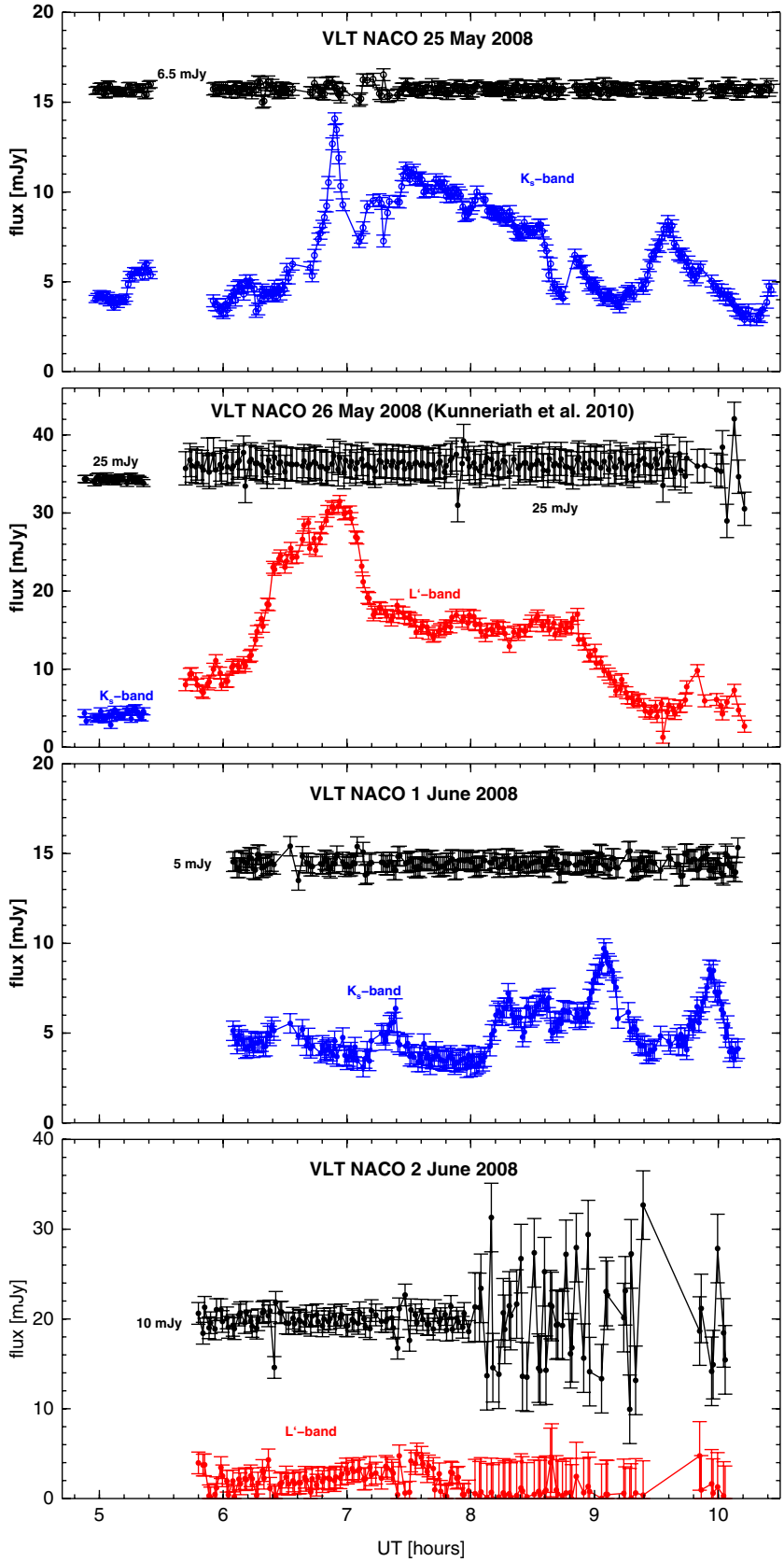

Figure 4. NACO VLT light curves for Sgr A* on a set of nights in 2008 May–June with no coordinated sub-mm observations. References for previously published flares are indicated. Blue and red represent *Ks* and L' bands, respectively. For a proper comparison with the *Ks* band, we have scaled the Sgr A* L'-band data by a factor 0.72, which corresponds to a spectral index of −0.6 (Hornstein et al. 2007). The corresponding calibration stars are shown in black. The number next to the VLT calibration stars represents an offset that has been added for representation purposes.

(A color version of this figure is available in the online journal.)

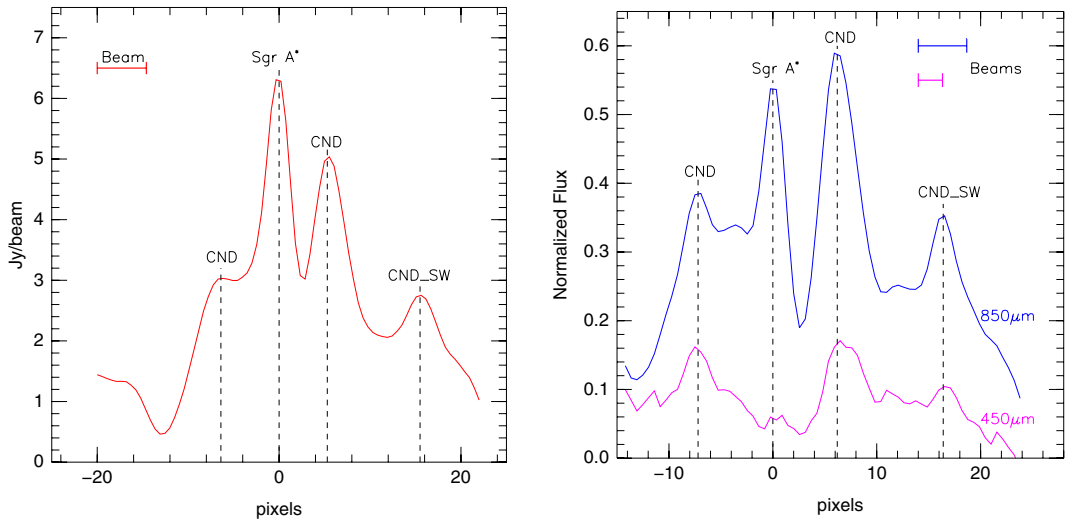

Figure 5. Left: intensity profile along the inner section of Figure 1, in a direction along the major axis of the CND. Sgr A*, the CND external envelope, and the region labeled as CND-SW are marked. Right: similar profiles along the inner section of the same line in the 450 and 850 μm SCUBA maps (see Figure 3). The fluxes have been normalized to the peak of each map, which is located in the 20 km s^{-1} cloud. Sgr A*, the CND external envelope and the region labeled as CND-SW are marked. (A color version of this figure is available in the online journal.)

to changes in the adopted dust emissivity than to temperature variations of the same order.

The molecular cloud masses are comparatively larger than those derived by Pierce-Price et al. (2000), who found a total mass for the CMZ (at 850 μm) of (53 $\pm$ 10) $\times$ 10^6 $M_\odot$. In the case of the CND, where we measure (7.9 $\pm$ 3.1) $\times$ 10^5 $M_\odot$, the situation gets complicated. Much effort has been invested to calculate its mass, but the fact is that different wavelengths and methods yield values with orders of magnitude difference. Using 31.5 and 37.3 μm maps, Latvakoski et al. (1999) derive the optical depth in the GC, and calculate a total mass traced in the FIR of 3.4 $\times$ 10^3 $M_\odot$, of which 1.3 $\times$ 10^3 $M_\odot$ belongs to the FIR ring surrounding the CND. Consistent with our result, they conclude that this ring traces only 13% of the total CND mass (10^4 $M_\odot$).

On the other hand, using HCN and HCO$^+$ measurements, Christopher et al. (2005) concluded that the total gas mass of the CND is about 10^6 $M_\odot$. This value is in agreement with the 1.3 $\times$ 10^6 $M_\odot$ total molecular mass quoted by Montero-Castaño et al. (2009) and, within the errors, is in agreement with our result.

It is worth mentioning that the CND mass should not be determined only from dynamical measurements. This is because the black hole mass (4.8 $\pm$ 1.0 $\times$ 10^6 $M_\odot$) is much larger than the whole range of suggested CND masses. Even for the largest mass estimates of the CND, the mass is comparable to the mass of the surrounding stars, and it would be very difficult to distinguish between them.

6. TEMPERATURE AND SPECTRAL INDEX DISTRIBUTION

We have used the JCMT 450 and 850 μm archive maps (see Figure 3) for calculating the temperature and spectral index maps in the inner parsecs of the GC region. This is included in the following sections, along with a morphological description of the SCUBA maps, and an objective comparison between the APEX 870 μm and SCUBA 850 μm data.

6.1. APEX 870 μm versus SCUBA 850 μm Extended Emission

One way of checking the reliability of the archive SCUBA maps is to compare the 850 μm map against the LABOCA map. Since the observations and data reduction have been completely independent, this comparison should give us a handle on the expected quality of the results derived with the SCUBA data.

Due to their wavelength proximity, the 870 μm LABOCA and the 850 μm SCUBA maps should in principle exhibit the same structures and flux levels. The differences found could then be attributed to differences in the data reduction (e.g., zero-point definition, filtering), or to observation technique effects (e.g., scanning artifacts).

From a purely morphological point of view, both maps are in good agreement: they show the same structures and approximately the same relative intensities (see Figures 1 and 3, right). The 20 and 50 km s^{-1} clouds, as well as the secondary clouds, are consistently traced. This accordance is also shown in the low surface brightness regions. In both maps, the central region is dominated by the variable source Sgr A*, along with the northern and southern lobes of the CND.

To quantify the comparison between both maps, we have estimated their percentage flux difference. To do that we first smoothed the higher resolution map (14$''$ at 850 μm) to the lower one (19$''$ at 870 μm). Afterward, both maps were aligned by minimizing the difference in the position of the individual clouds, clipped below 0.8 Jy to avoid very low flux contributions (presumably sources of error), and subtracted. Negative fluxes in the most external low surface brightness regions are one characteristic of these SCUBA maps; they are most likely systematic effects from the deconvolution/large-scale filtering. This difference was finally transformed into a percentage value. As shown in Figure 6, most of the regions studied exhibit a high level of agreement ($\pm$0%–25%). As for the rest of the map, it shows that there are flux differences from 25% to more than 100%. However, these large values are generally associated with low surface brightness regions (see also Figure 1), and with regions with high flux contrast.

This comparison shows that for many regions the two long-wavelength maps are in good agreement (25% or better). It also indicates that the use of the 450 μm data will most likely provide information on the true underlying flux ratios in those same regions of the map. Therefore, we decided to consistently derive both the temperature and spectral index maps using only

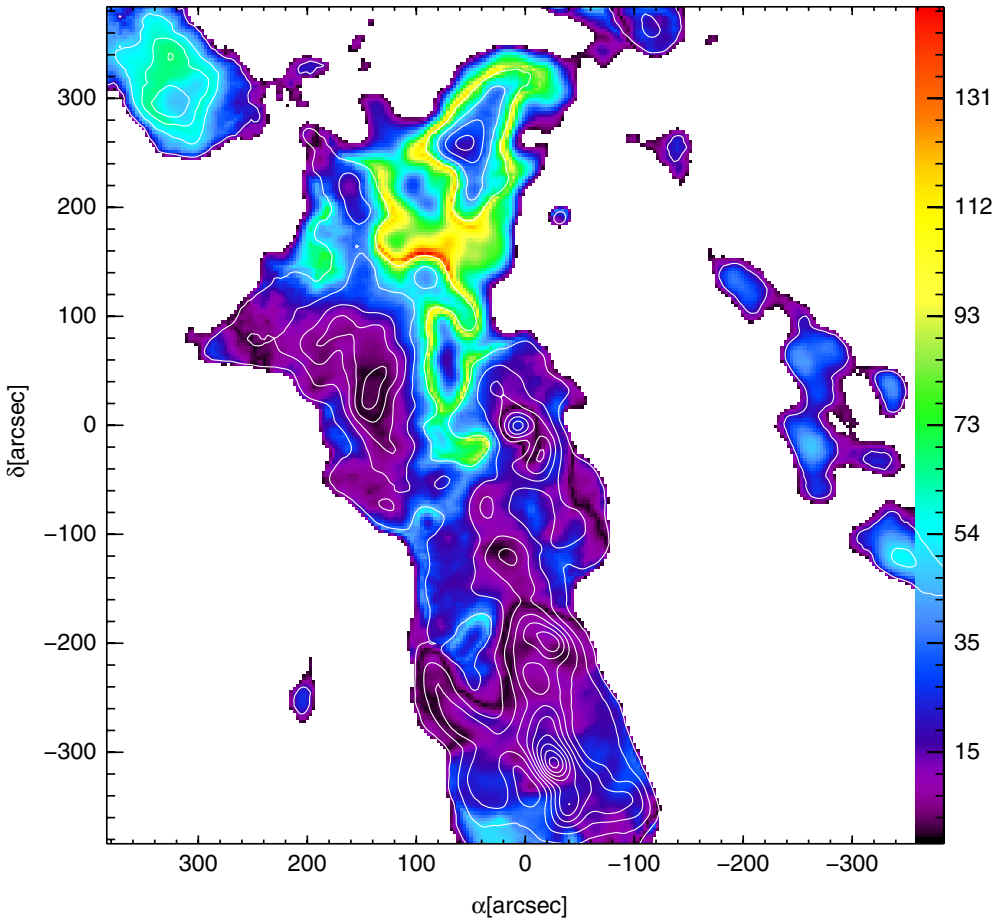

Figure 6. Difference between the LABOCA 870 μm and the SCUBA 850 μm maps expressed in percent. White contours represent the LABOCA map, with levels 2, 3, 4, 5, 6, 7, 8, 9, and 10 Jy beam^{-1}.

(A color version of this figure is available in the online journal.)

the SCUBA data in the regions where the agreement with the LABOCA map is 25% or better.

Finally, the LABOCA and SCUBA maps both show differences in flux with respect to the 850 μm map from Pierce-Price et al. (2000). In their 850 μm SCUBA map, a flux density of about 5.5–6.6 Jy beam^{-1} is assigned to the outer regions of the 20 and 50 km s^{-1} clouds. Being conservative, as the comparison is somewhat qualitative, in the LABOCA map these same regions start approximately in the contour level 3 Jy beam^{-1}, whereas in the SCUBA map they start approximately at the contour level 2 Jy beam^{-1}. We believe that these differences may be due to the data reduction process, in particular to the large-scale applied filtering.

6.2. 450 and 850 μm Extended Structure

The 450 and 850 μm SCUBA maps consistently trace the structure of the molecular clouds in the GC. It is in the CND and CND-SW regions where their differences are remarkable. While Sgr A*, the CND, and surroundings are shown as bright structures at the longer wavelength, at shorter wavelengths their emission is very weak. At 450 μm, Sgr A* has an upper flux limit level of about 2.5–3.0 Jy, and it is not clearly detected as a point source (see comparison in Figure 5, right). The CND lobes exhibit emission peaks about three times brighter than that corresponding to Sgr A*. The CND-SW source is also detected with a relative flux about 1.5 times larger than that associated with Sgr A*. This low-level emission from the very central regions is somewhat striking (though previously observed with SCUBA maps, e.g., Pierce-Price et al. 2000). One would expect the emissivity and thus the opacity to be larger at the shorter wavelength, so the intensity should be stronger. It is of course possible to argue that there are problems in the map itself, in the zero flux level, or in the instrument which may lead to a non-detection of the point source, Sgr A*. However, this is an unlikely explanation, since all other bright point-like sources present in the region are detected, and no negative fluxes in the CND region have been measured. The low flux level may have a higher impact in secondary structures, but on the other hand their morphology coincides well with the longer wavelength maps. Furthermore, these results agree with those of Dent et al. (1993), who used the UKT14 bolometer at the JCMT, and obtained a detailed map of the region at 450 μm. They do not detect emission at the position of Sgr A*, giving an upper limit to the 450 μm flux of 1.5 Jy. Within the uncertainties, this value is in agreement with our previously mentioned flux limit, especially considering the variable nature of the source. Consistent with the SCUBA map (see Figure 3), Dent et al. (1993) measure the flux peak of the CND lobes to be about 9 Jy beam^{-1}. This low surface brightness emission at the shorter wavelength can be interpreted as an indication of lower temperatures in the CND region than in the rest of the molecular clouds. This is surprising, since this area is close to abundant heating sources. Another possible explanation is that mechanisms other than thermal emission may produce this

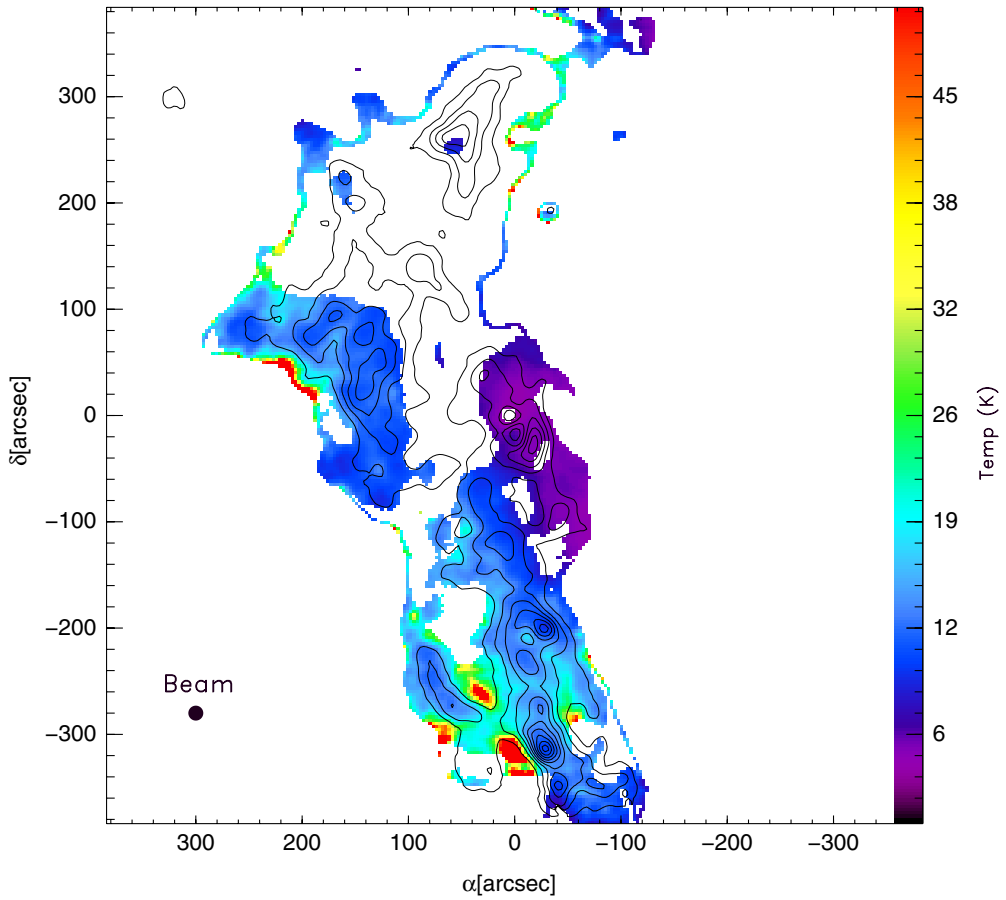

Figure 7. Temperature map derived using the JCMT 450 and 850 μm maps. We have only used high-confidence regions derived from the LABOCA–SCUBA comparison (see Figure 6). Black contours represent the 850 μm map with values 2, 3, 4, 5, 6, 7, 8, 9, and 10 Jy beam^{-1}. The emission from regions with temperatures apparently lower than 10 K is likely to be dominated by a mixture of emission mechanisms. North is up, east to the left.

(A color version of this figure is available in the online journal.)

continuum. The analysis of the physical mechanisms giving rise to these sub-mm structures will be important for interpreting these observations (see Section 6.4).

6.3. Temperature Distribution in the Galactic Center

We have derived a temperature map of the GC central parsecs using only the regions of the SCUBA maps whose fluxes are consistent, within 25%, with the LABOCA ones. This also guarantees a signal higher than a $\sim 2\sigma$ level over the estimated rms of the map. Sgr A* is then excluded from the temperature analysis, although the high error may well be due to the variable nature of the source that gives different flux density values in different observing runs.

Our basic assumption is that the cold dust emission is optically thin at 450 and 850 μm. This can be justified on two grounds. First, the column density required to have opacity 1 at these wavelengths would be too large to be consistent with the known gas column densities. Second, the brightness temperature of the sub-mm emission is far below the dust temperature, even after the surface filling factor is taken into account. Therefore, the dust temperature can be determined from the ratio of the fluxes at two different wavelengths. At temperatures of about 10 K, the blackbody emission peaks at about 500 μm; thus the Rayleigh–Jeans approximation is not applicable for the current data. Therefore, the flux ratio will depend on the value of the emissivity spectral index β (which we assume to be 2.0, the theoretical maximum for crystalline dust grains; see Pierce-Price et al. 2000) and the temperature in the following way (see Kramer et al. 2003; Schnee & Goodman 2005):

$$\frac{S_{450}}{S_{850}} = \left(\frac{850}{450}\right)^{3+\beta} \frac{\exp(17\,\mathrm{K}/T_{\mathrm{dust}}) - 1}{\exp(32\,\mathrm{K}/T_{\mathrm{dust}}) - 1}. \quad (3)$$

Since the temperature is based on a flux ratio (i.e., is a relative measurement), we consider that systematic effects due to the data reduction, filtering, etc., will be smeared out and that they will not have an important impact in our calculations. The flux ratio will of course not account for variations like those caused by the observing weather conditions: high opacities would affect 450 μm more than the 850 μm flux measurements, and may therefore have an impact in the results. In any case, even if the absolute temperature measurements are affected by the data treatment, the relative variations in temperature can be safely investigated. The SCUBA maps have different beam sizes, about 7″ and 14″ for the 450 and 850 μm maps, respectively. To properly compare the maps and derive the temperatures, we smoothed the higher resolution map to the lower one.

The temperature map derived is presented in Figure 7, with values ranging from approximately 5–25 K in the regions under study. The comparison with the 850 μm continuum contours shows an anti-correlation between the flux density and the temperature: the low surface brightness regions are the warmest ones, whereas the bright molecular clouds and the CND regions

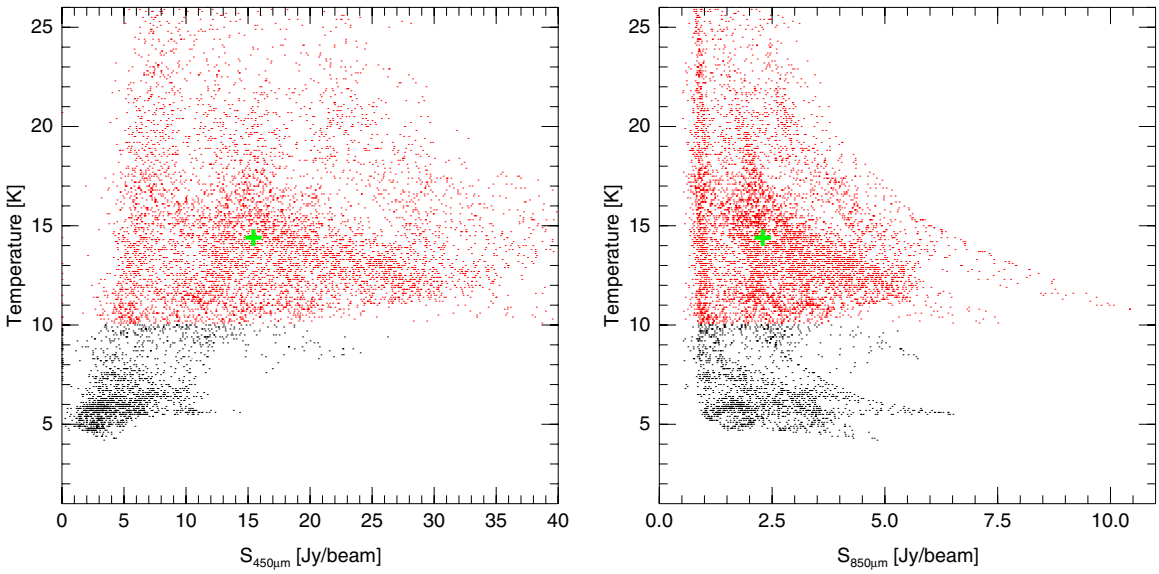

Figure 8. Left: temperature and 450 μm flux distribution corresponding to the map shown in Figure 7. The red and black clouds separate, respectively, temperatures equal and larger, or lower than 10 K. The green cross located in the red cloud indicates its median value for the temperature (14.4 K) and flux (15.4 Jy beam^{-1}). Right: same as at left but for the 850 μm flux distribution. Here the temperature and flux median values are 14.4 K and 2.3 Jy beam^{-1}, respectively.

(A color version of this figure is available in the online journal.)

and surroundings are colder. The regions of the 20 and 50 km s^{-1} molecular clouds analyzed have dust temperatures ranging between 10 and 20 K, with the 850 μm maxima tracing the low temperatures. This is consistent with dust emission being the dominating mechanism. The median temperature, calculated only in regions where $T \geqslant 10$ K (see Figure 8), is about 14 ± 4 K. This number compares well, within the uncertainties, with the 21 ± 2 K given by Pierce-Price et al. (2000) for a larger area of the GC, but it is about half the average 30 K estimated by Lis et al. (1991), which we used for the mass derivation. As an example, a temperature decrease of about 10 K would increase the derived mass by a factor of about 1.7. Before re-calculating the masses we have to consider that our temperature map does not cover all the clouds analyzed and that, as we will see below, some temperatures are quite uncertain. Therefore, we decided to keep the previously used 30 K as a temperature average for the mass calculation.

The apparently coldest regions (<10 K) are mainly located in the CND and its surroundings, with the region encompassing Sgr A* being one of the coldest. There are other small areas with low temperatures, but they are mainly in the outskirts of the area studied. Here the temperature determination may be affected by border effects. This result for the CND is surprising, since one would expect the temperatures there to be the highest ones, and contradicts the conclusions of Latvakoski et al. (1999). Using 31.5 and 37.7 μm maps, these authors found that the color temperature in the internal region of the CND was higher than in the surroundings by about 100 K. It is also in contradiction with the conclusions of the 50 and 90 μm work of Davidson et al. (1992), who found dust temperature between 40 and 70 K in the CND–CND-W region, with the peak located in the close vicinity of Sgr A*.

Our formally derived cold temperatures (below 10 K) are too low and should be considered unphysical. There are two likely explanations for this. The first is that we are dealing with optical depth effects, and it may happen that the emission is not optically thin in all areas, misleading the temperature calculations. The second explanation is that those areas may not be dominated by thermal (dust) emission, and the procedure used to derive the temperature is therefore not applicable.

The first explanation can be cross-checked using the flux–temperature distribution. For the 450 μm continuum map, the distribution has a well-defined projected cone-like shape with its outer envelope showing a tendency for increasing temperature with flux (Figure 8, left). In contrast, the distribution of the 850 μm points does not show such a clear pattern, and the outer envelopes do not reveal any particular trend (Figure 8, right). There are in fact regions with the highest fluxes (>5 Jy beam^{-1}) and very low temperatures (~6 K). On the other hand, the flux peaks of the map present temperatures above 10 K (see Figure 7). Therefore, we do not have enough evidence to conclude that optical depth effects are responsible for the apparently (very) cold dust measurements. As for the possibility of non-thermal emission in the GC region, this will be analyzed in the next subsection as part of the discussion of the spectral indices.

6.4. The Spectral Indices Distribution: Physical Mechanisms at Work in the Inner parsecs

We have generated a detailed spectral index distribution (see Figure 9) using the 450 and 850 μm SCUBA maps, with the same smoothing and clipping used for the temperature distribution. The spectral indices are derived via the expression

$$\alpha = \frac{\log(S_{450\mu m}/S_{850\mu m})}{\log(\nu_{450\mu m}/\nu_{850\mu m})}. \quad (4)$$

The morphology of this map is of course equivalent to that of the temperature. However, it is useful to show the map in order to analyze the derived α and discuss the results more easily. In general, the spectral index has values equal to or larger than 2, indicating that the 20 and 50 km s^{-1} clouds are mostly dominated by thermal emission. This is consistent with the Pierce-Price et al. (2000) results: they have already discussed the emission from dust as the principal mechanism dominating these two clouds. Nonetheless, their spectral indices values are

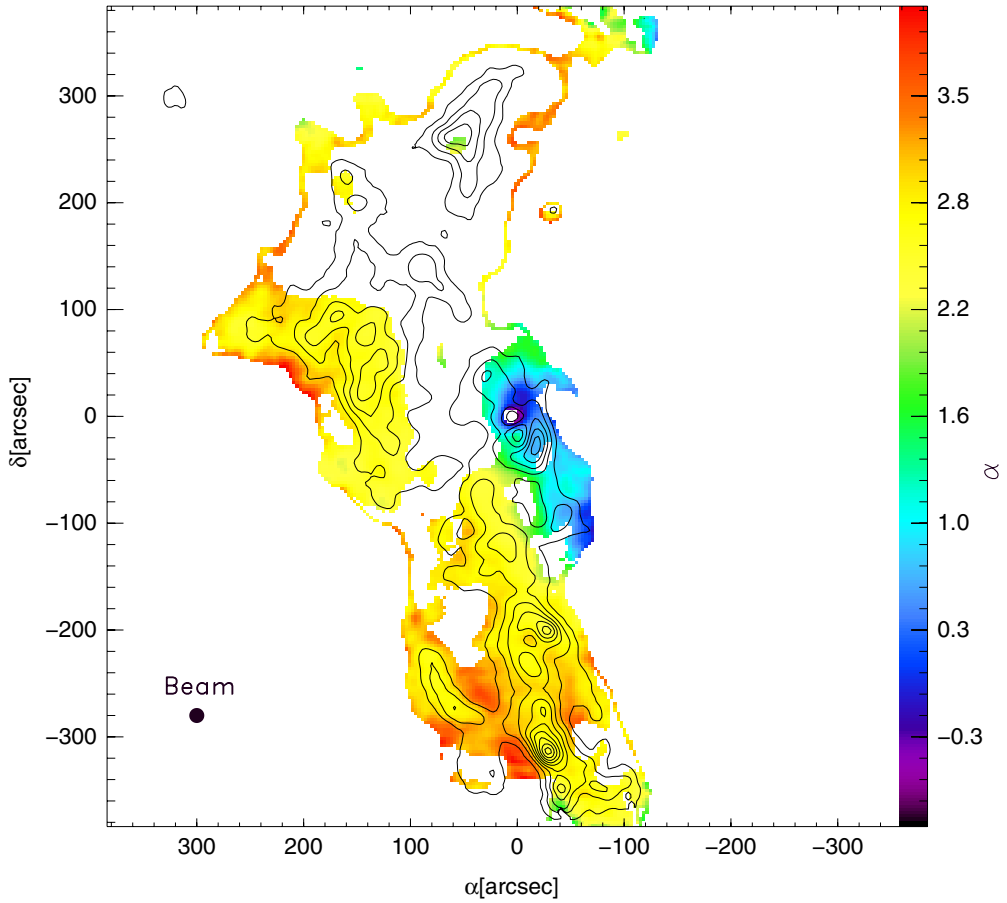

Figure 9. Map of the spectral index, α, over the GC regions covered by the JCMT 450 and 850 μm data. We have only used high-confidence regions derived from the LABOCA–SCUBA comparison (see Figure 6). Black contours represent the 850 μm map with values 2, 3, 4, 5, 6, 7, 8, 9, and 10 Jy beam^{-1}. North is up, east to the left.

(A color version of this figure is available in the online journal.)

about 1.2 times larger than ours. As mentioned before, this is probably due to the different data reduction processes and their correction for artifacts, which we have not applied.

A direct comparison between the temperature map (Figure 7) and the spectral index distribution (Figure 9) shows that areas associated with excessively low temperatures also have low spectral indices, ranging from −0.6 to 1.0. In the CND and surrounding areas, we have defined three different spectral index regions: from east to west, these represent a radial decrease toward Sgr A*. The first region, with α values between 1 and 2, partially occupies the CND. We can therefore explain the measured spectral indices with equal contributions of synchrotron and dust emission, and a 30% synchrotron and 70% dust contribution. In this calculation 3 is assumed to be the typical spectral index for the dust emission, and a steep −1 for the synchrotron (Sgr A East α values derived from radio data range from −0.5 to about −1.0; Ekers et al. 1983).

Further inward to Sgr A*, the spectral index ranges between 0 and 1. This can be explained with a combination of synchrotron emission ($\alpha \sim -0.75$) contributing between 20% and 45% and dust emission ($\alpha = 3.0$) contributing between 80% and 55%.

Closer to the GC itself, and surrounding Sgr A*, we measure a halo structure with about $-0.6 < \alpha \leqslant 0.0$, which can be explained with a combination of 90%–70% synchrotron emission and 10%–30% dust and free–free. For the regions surrounding Sgr A*, VLA radio maps at 6 and 20 cm wavelength have been obtained by Yusef-Zadeh & Morris (1987b). They show that we can expect a surface brightness of ∼1 Jy in the 14″ FWHM diameter beam area around Sgr A* that is covered by the SCUBA telescope at 350 GHz. Assuming a spectral index of −0.5, this results already in a contribution of non-thermal radiation of 0.12 Jy at 350 GHz. A significant portion of non-thermal 350 GHz radio emission may also be associated with compact pulsar/neutron stars and their winds. Muno et al. (2008) explained the diffuse X-ray emission in the central 10″–15″ of the *Chandra* map as being dominated by non-thermal emission from a few tens of pulsar/neutron star winds.

In addition to pulsar winds that are extended on the arcsecond scale, we may also expect a contribution from compact non-thermal radio emission from jet components associated with pulsars and neutron stars (e.g., Pestalozzi et al. 2009; Dubner et al. 2008; Migliari et al. 2007). Here we assume that emission of the order of 1 Jy at 350 GHz can be explained by a few tens of sources with flux densities at the synchrotron self-absorption peak of about ⩽0.2 Jy each. For compact objects with a size of 0.1–0.3 mas (4–12 × 10^{-6} pc) diameter and a magnetic field of 1–100 G averaged over the corresponding source volume, one obtains an synchrotron self-absorption turnover at 20–50 GHz. Given this turnover frequency, this assumption is in agreement with an upper limit from these compact sources of 3 mJy at 5 GHz (see the discussion in Muno et al. 2008). It would also

be in agreement with high-resolution 100 GHz and 230 GHz CARMA interferometry maps of the mini-spiral region that do not detect compact sources (e.g., IRS13; Kunneriath et al. 2010).

Finally, Sgr A* itself has been left out of the spectral indices analysis, due to the inconsistency between the LABOCA and SCUBA results.

In summary, we find a significant contribution of non-thermal emission in the GC region, especially in the CND and surroundings: the spectral index gets steeper as we approach Sgr A* itself.

For the present analysis we have relied on the SCUBA data, and on the fact that the flux ratio should give a stable result, reasonably independent of the data reduction process. However, to test the validity of our results, we have calculated how variations in flux (derived from the data analysis; see Section 3.1) would affect our results. We find that, if the percentage of missing flux is the same in the two wavelengths, the result will be obviously the same. In the unlikely scenario that only the 450 μm flux has up to 100% flux missing, the thermal emission will dominate more as the 450 μm flux increases, but still the spectral index values will decrease toward the nuclear regions. The spectral index value in the central region will go from steep to flat in the Sgr A* regions as the percentage of missing short-wavelength flux increases. The inverse situation occurs when we consider that only the 850 μm map has missing flux and account for it. This results in an unlikely scenario where the thermal emission becomes less important (even in the molecular clouds) as the long-wavelength flux increases. However, a decrease on the spectral index toward the center is again measured. Finally, if we consider that in both wavelength regimes there is some flux missing, the steeper spectral index in the central region is still detected. For instance, a 30% and 50% increase in the long- and short-wavelength fluxes, respectively, would imply an increase of only 0.2 in α.

This test confirms that, in the sub-mm domain, the CND and surrounding regions are not purely thermally dominated. Therefore, the temperature calculations given in Section 6.3 are not valid for these regions, and the low temperatures obtained are not representative of their physical conditions. To properly disentangle all the proposed mixed mechanisms in adequate ratios, further data would be needed. Quasi-simultaneous multi-frequency measurements using APEX or ALMA will help to further constrain the scenario played here.

7. Sgr A* LIGHT CURVES

7.1. General Characteristics

In the center of all these complex molecular clouds and streamers lies Sgr A*, the true GC. In the previous part of this paper we have attempted to understand the environment that surrounds Sgr A*, and the main physical mechanisms taking place there. In the following we will not only concentrate on the characterization of the Sgr A* variability, which is key to understanding the processes taking place there, but we will attempt to define a classification scheme for the different types of flares.

The complete set of NIR and sub-mm light curves obtained in the 2008 coordinated VLT–APEX campaign, along with the complementary Subaru data, is presented in Figures 2 and 4. We have NIR data for nine nights and sub-mm data for five. Coordinated observations between APEX, VLT, and Subaru were possible on two nights and between APEX and Subaru for one night of the observing run. However, as we will see in Section 8.3, the APEX and Subaru sites make the synchronism fail, and the light curves are not suitable for modeling. Throughout the text, we define the activity of Sgr A*, or flare, as the presence/occurrence of significant flux density excursions. For instance, a minimal variation of 4σ above the quiescent level in 15 minutes (Bremer et al. 2011) can be used to define a flare. However, this definition is not unambiguous, and no distinct flare description can be found in the literature.

Due to the expansion velocity postulated in the adiabatic expansion model (see Section 8.2), the sub-mm light curves are expected to be broad, since the individual components are mixed and overlap with each other. In the case of the sub-mm light curves, the median activity peak and offset are 4.3 ± 0.4 Jy and 2.9 ± 0.4 Jy, respectively. The total flare length and peak time are in general not well determined; this is due to the insufficient time coverage of the available data. At most, we can state that the lower limit for the sub-mm flare duration is about 3 hr.

7.2. NIR Light-curve Description and Classification

The main observational features of the light curves are detailed in Table 4. For each night, these measurements have been derived directly from the observed (discrete) NIR and sub-mm light curves. The values presented are the activity peak and the light-curve minimum, which can be considered as an offset. This offset is meant to distinguish between rapid intra-day variability, and variability that may occur at longer timescales. The activity length and activity start and peak are also shown. We define activity start as the time when the flux increases and no longer shows stable behavior.

The NIR light curves present an average flux density of the flare maxima of 14.1 ± 5.5 mJy, with a typical light-curve minimum of 2.9 ± 2.9 mJy. The average activity length is 5.3 ± 0.7 hr. There is no common or very specific structure for the NIR light curves of Sgr A*. Some of them are dominated by a well-defined main flare, whereas others appear to be formed by short-time events with no clear dominant flare underneath. These flux density variations (i.e., the light-curve structure) can be explained in a disk or jet model (see, e.g., the discussion in Eckart et al. 2006a, 2006b, 2008a). They could also be explained as a consequence of an underlying physical process that can be described as continuous red noise variations (e.g., Do et al. 2009).

Up until now, a classification scheme to categorize the NIR flares has not been defined. However, it would be useful to have a systematic method for separating the light curves according to their structure and activity level. We propose a classification scheme where the observed light curves are defined with a combination of individual short events (i.e., hot spots) and an underlying transient small disk (Meyer et al. 2006a). The proposed classes are as follows.

1. *Type I*. Clustered events with a clear underlying flare. In this case the flare substructure would be due to relativistic events orbiting around the black hole, whereas the main underlying flare is due to instabilities in the underlying transient disk (Meyer et al. 2006a). The (main) flare duration is of the order of one hour or more, with a peak intensity of between 5 and 30 mJy. The main flare, which in general has a Gaussian-like shape, has to clearly go up and down. The sub-flares, with a duration of the order of 20 minutes, are overimposed in the main flare, and generally their structures do not dominate the flare shape. Within the Type I flares there is one outstanding type. It is characterized by an initial steep ($\geqslant$10 mJy) rise followed by a smooth decay

Table 4
Characteristics of the NIR and Sub-mm Sgr A* Light Curves

Flare ID	Band (Telescope)	Activity Peak[a]	Offset[b]	Activity Length[c]	Activity Start[c]	Activity Peak[c]
25_05_08	*Ks* (VLT)	14.1	2.9	5.4	5.0	6.9
26_05_08[d]	L'/Ks (VLT)[e]	31.5	2.0	5.3	4.9	6.9
27_05_08	*Ks* (VLT)	5.8	2.2	3.5	4.9	6.5
27_05_08	*Ks* (Subaru)	6.9	2.0	>1.0	<10.8	10.8
28_05_08	*Ks* (VLT)	7.4	3.8	∼1.0	8.6	9.1
28_05_08	*Ks* (Subaru)	11.8	3.1	>1.5	∼12.5	13.4
29_05_08[f]	*Ks* (Subaru)	7.7	1.0	3.6	9.4	12.0
30_05_08	L'/Ks (VLT)	16.5	∼0.0	5.0	5.7	8.4
01_06_08	*Ks* (VLT)	9.7	3.1	4.1	6.1	9.1
02_06_08	L' (VLT)	5.0	∼0.0	0.0	...	...
03_06_08[g]	L'/Ks (VLT)[e]	29.8	∼0.0	5.3	<4.7	5.4
27_05_08	sub-mm (APEX)	4900.0	3200.0	3.6	<7.0	7.4
28_05_08	sub-mm (APEX)	4300.0	2952.0	3.7	<7.1	8.7
29_05_08	sub-mm (APEX)	3000.0	1841.0	0.9	∼10.0	10.8
30_05_08	sub-mm (APEX)	4260.0	3600.0	1.1	<8.3	8.4
03_06_08[g]	sub-mm (APEX)	4530.0	3400.0	4.1	6.2	6.7

Notes.
[a] Estimated activity peak. Units are mJy.
[b] Light-curve minimum, which can be considered as an offset. Units are mJy.
[c] Units are UT (hours).
[d] Kunneriath et al. (2010).
[e] L'-band flux peak value given is scaled by a factor 0.72.
[f] Nishiyama et al. (2009a).
[g] Eckart et al. (2008b).

or a plateau, followed by a milder activity peak (e.g., 2008 May 25 and 26 flares; see Figure 4). These flares are strong and last for several hours. Within the already published flares, there is no case with the inverse structure (smooth rise and final very steep decay). This is because the dissipation time is longer than the disturbance time, and thus the initial steep rise must be followed by a slower decay.

2. *Type II*. Clustered but still discernible individual events, which could be explained as short (about 20 minutes) and frequent localized events whose intensity may vary from a few up to a 40 mJy peak (e.g., 2008 May 30 and June 1; see Figures 2 and 4). The time separation between these events is typically $\lesssim$30 minutes.
3. *Type III*. Short (about 20 minutes) localized individual events. This flare type is similar to Type II, but here the frequency of events in not that high, and thus they are separated from each other by more than 30 minutes (e.g., 2008 May 27, 28, and 29; see Figure 2).
4. *Type IV*. No flare activity. Sgr A* is in a quiescent phase.

We have used this method to classify a large number of published NIR Sgr A* light curves (see Table 5). Including the ones presented in this paper, a total of 90 flares obtained in different facilities have been classified. 11% of flares could not be properly classified, mainly due to the time coverage. In addition to this, 18% of flares have been tentative classified. This is mainly because the light-curve time sampling and/or the display chosen by the authors prevented a clear assessment of the flare type. From the remaining 64 light curves, 14% belong to Type I, 27% and 12% to Types II and III, respectively, and 47% to Type IV. Hence, strong variability episodes with an underlying main flare represent about one-sixth of the classified flares, whereas short individual events, either clustered or sparse, are the most common activity types. Sgr A* presents a quiet state in almost 50% of cases. Further unbiased statistics which make use of all observed light curves rather than only the active ones (e.g., *H*-band light curves in Bremer et al. 2011) are needed to better constrain these results.

8. Sgr A* VARIABILITY: SSC SOURCES IN ADIABATIC EXPANSION

One of the most relevant characteristics of Sgr A* is its variability through the different spectral regimes. All attempts to model and understand the nature of this source should properly account for this. In this context, the variability events can be divided into two classes: simultaneous or not. There is observational evidence indicating that the NIR/X-ray flares are synchronous events, pointing toward the same population of electrons being responsible for the emission at both wavelengths. Radio/sub-mm flares, on the other hand, appear to be systematically delayed with respect to the NIR/X-ray ones. This also indicates that there has to be some correlation between these events.

To understand the Sgr A* activity different interpretations, models, and explanations have been proposed by several authors. One of the models already proposed combines the description of an adiabatically expanding cloud with the additional constraint of a synchrotron self-Compton (SSC) formalism (see Eckart et al. 2008b; Sabha et al. 2010). Other authors have also claimed the possibility of a relation between the observed flares in these wavelength regimes (e.g., Yusef-Zadeh et al. 2006, 2009). However, this is still an open question, since these flares may be unrelated, and events producing isolated sub-mm flares are also plausible (Falcke et al. 2009; Maitra et al. 2009). Alternatively, there have been efforts to interpret the NIR variability of Sgr A* as a consequence of an underlying physical process that can be described as continuous red noise variations (e.g., Do et al. 2009). More recently, Zamaninasab et al. (2010) have correlated the modulations of the intensity light curves and changes in polarimetric data, and modeled them with a relativistic hot spot model.

Table 5
Classified Light Curves

Date	Band/Instrument	Telescope	Class	Reference
2002 Aug 30	L'/NACO	VLT	∼	Gen03
2003 Mar 19	H/NACO	VLT	IV	Bre11
2003 May 9	H/NACO	VLT	∼	Gen03
2003 Jun 14	H/NACO	VLT	IV	Bre11
2003 Jun 15	H/NACO	VLT	IV	Bre11
2003 Jun 15	K/NACO	VLT	I	Gen03
2003 Jun 16	H/NACO	VLT	IV	Bre11
2003 Jun 16	K/NACO	VLT	I	Gen03
2003 Jun 20	Ks/NACO	VLT	∼	Eck04
2003 Jul 21	H/NACO	VLT	IV	Bre11
2003 Sep 5	H/NACO	VLT	IV	Bre11
2003 Sep 6	H/NACO	VLT	IV	Bre11
2004 Apr 29	H/NACO	VLT	∼	Bre11
2004 Jun 11	H/NACO	VLT	IV	Bre11
2004 Jun 12	H/NACO	VLT	IV	Bre11
2004 Jun 13	K_s/NACO†	VLT	II	Eck06a
2004 Jul 6	HKL'/NACO	VLT	IV	Eck06b
2004 Jul 7	K/NACO	VLT	II	Eck06b
2004 Jul 7	NIRC2	Keck2	II/III:	Mey09
2004 Jul 8	H/NACO	VLT	IV	Bre11
2004 Jul 8	$L'K$/NACO	VLT	II	Eck06b
2004 Jul 8	NIRC2	Keck2	II/III:	Mey09
2004 Jul 29	H/NACO	VLT	IV	Bre11
2004 Aug 30	K/NACO	VLT	IV	Sab10
2004 Sep 23	K/NACO	VLT	IV	Sab10
2004 Aug 29	H/NICMOS	*HST*	III/IV:	Yus06
2004 Aug 30	H/NICMOS	*HST*	I/II:	Yus06
2004 Aug 31	H/NICMOS	*HST*	III/IV:	Yus06
2004 Sep 1	H/NICMOS	*HST*	I/II:	Yus06
2004 Sep 2	H/NICMOS	*HST*	III/IV:	Yus06
2004 Sep 3	H/NICMOS	*HST*	I/II:	Yus06
2005 May 16	H/NACO	VLT	II	Bre11
2005 Jun 18	K/SINFONI	VLT	II	Gui06
2005 Jul 16	L'/NIRC2	Keck2	∼	Hor07
2005 Jul 28	L'/NIRC2	Keck2	II	Do09
2005 Jul 30	K_s/NACO†	VLT	II	Eck06a
2005 Jul 31	$HK'L'$/NIRC2	Keck2	I	Hor07
2006 Apr 29	H/NACO	VLT	IV	Bre11
2006 May 2	$HK'L'$/NIRC2	Keck2	IV	Hor07
2006 May 3	K'/NIRC2	Keck2	II	Do09
2006 May 31	H/NACO	VLT	IV	Bre11
2006 Jun 1	K_s/NACO†	VLT	I	Mey06b/Zam10
2006 Jun 13	H/NACO	VLT	∼	Bre11
2006 Jun 29	H/NACO	VLT	IV	Bre11
2006 Jun 20	K'/NIRC2	Keck2	II	Do09
2006 Jun 21	K'/NIRC2	Keck2	II	Do09
2006 Jul 17	K'/NIRC2	Keck2	∼	Hor07
2006 Jul 24	H/NACO	VLT	IV	Bre11
2006 Jul 27	H/NACO	VLT	IV	Bre11
2006 Aug 28	H/NACO	VLT	IV	Bre11
2006 Sep 16	H/NACO	VLT	IV	Bre11
2006 Oct 03	H/NACO	VLT	II	Bre11
2006 Oct 15	H/NACO	VLT	IV	Bre11
2007 Mar 17	H/NACO	VLT	II	Bre11
2007 Jul 19	H/NACO	VLT	IV	Bre11
2007 Jul 21	H/NACO	VLT	IV	Bre11
2007 Aug 12	K'/NIRC2	Keck2	IV	Do09
2007 Apr 1	KL'/NACO‡	VLT	III	Dods09
2007 Apr 2	K/NACO	VLT	IV	Dods09
2007 Apr 3	KL'/NACO‡	VLT	III	Dods09
2007 Apr 4	HKL'/NACO‡	VLT	I	Dods09
2007 Apr 5	KL'/NACO†	VLT	III	Dods09
2007 Apr 6	KL'/NACO‡	VLT	III	Dods09
2007 Apr 1	F145M, F170M/NICMOS	*HST*	III:	Yus09
2007 Apr 2	F145M, F170M/NICMOS	*HST*	III:	Yus09
2007 Apr 3	F145M, F170M/NICMOS	*HST*	III:	Yus09
2007 Apr 4	F145M, F170M/NICMOS	*HST*	III:	Yus09
2007 Apr 5	F145M, F170M/NICMOS	*HST*	III:	Yus09
2007 Apr 6	F145M, F170M/NICMOS	*HST*	III:	Yus09
2007 Apr 7	F145M, F170M/NICMOS	*HST*	III:	Yus09
2007 May 15	K/NACO†	VLT	II	Eck08a
2007 May 16	K_sL'/NACO	VLT	III	Kun10
2007 May 17	K_sL'/NACO†	VLT	I	Zam10
2007 May 18	L'/NACO	VLT	IV:	Kun10
2007 May 19	K_s/NACO	VLT	I	Kun10
2008 May 25	K_s/NACO	VLT	I	This work
2008 May 26	K_sL'/NACO	VLT	I	Kun10
2008 May 27	K_s/NACO	VLT	III	This work
2008 May 27	K_s/CIAO†	Subaru	∼	This work
2008 May 28	K_s/NACO	VLT	III	This work
2008 May 28	K_s/CIAO†	Subaru	∼	This work
2008 May 29	K_s/CIAO†	Subaru	III	Nis09
2008 May 30	K_sL'/NACO	VLT	II	This work
2008 Jun 1	K_s/NACO	VLT	II	This work
2008 Jun 2	L'/NACO	VLT	IV	This work
2008 Jun 3	KL'/NACO	VLT	II	Eck08b
2008 Jun 21	H/NACO	VLT	IV	Bre11
2008 Jun 22	H/NACO	VLT	IV	Bre11
2008 Aug 5	K_s/NACO	VLT	II	Dods11
2007 May 18	K'/NIRC2	Keck2	∼	Do09

Notes. (∼): Due to lack of information (i.e., short or inconvenient time coverage), the flare cannot be classified. (:) Tentative classification. The flare time sampling and/or the display chosen by the authors prevent a clear assessment of the flare type. †: Data taken in polarimetric mode. ‡Some K-band data used polarimetric mode. Gen03 (Genzel et al. 2003); Bre11 (Bremer et al. 2011); Eck04 (Eckart et al. 2004); Gui06 (Gillessen et al. 2006); Eck06b (Eckart et al. 2006b); Eck06a (Eckart et al. 2006a); Mey09 (Meyer et al. 2009); Sab10 (Sabha et al. 2010); Yus06 (Yusef-Zadeh et al. 2006); Hor07 (Hornstein et al. 2007); Do09 (Do et al. 2009); Mey06b (Meyer et al. 2006b); Zam10 (Zamaninasab et al. 2010); Dods09 (Dodds-Eden et al. 2009); Yus09 (Yusef-Zadeh et al. 2009); Eck08a (Eckart et al. 2008a); Kun10 (Kunneriath et al. 2010); Eck08b (Eckart et al. 2008b); Nis09 (Nishiyama et al. 2009a); Dods11 (Dodds-Eden et al. 2011).

This paper uses a model in which synchrotron and SSC components are sitting on a temporary accretion disk. The source components peak at frequencies of a few 100 GHz, are then upscattered by SSC processes to the NIR/X-ray regimes, and finally expand adiabatically to produce the delayed radio/sub-mm emission. For optically thin synchrotron emission we refer throughout this paper to photon spectral indices (α) using the convention $S_\nu \propto \nu^{-\alpha}$, where S_ν is the flux density at a certain frequency ν, and to spectral indices (p) of the electron power-law distributions using $N(E) \propto E^{-p}$, where $p = (1 + 2\alpha)$ for synchrotron emission.

8.1. Synchrotron Self-Compton Emission and Model

The SSC formalism applied has been explained extensively in Sabha et al. (2010). Here only the basics are given.

Following the terminology of Gould (1979) and Marscher (1983), we define a synchrotron source of angular size θ (a few Schwarzchild radii). It is assumed that the emitting electrons follow a power-law distribution,

$$N(E) = N_0 E^{-(2\alpha+1)} (\gamma_1 mc^2 < E < \gamma_2 mc^2), \quad (5)$$

where γ_1 and γ_2 are the minimum and maximum electron Lorentz factors. A γ_2 value of the order of 10^3 is desired to obtain enough SSC in the X-ray domain. α represents the optically thin spectral index. We define the cutoff or turnover frequency ν_m as that where the synchrotron source becomes optically thick. Considering the relativistic bulk motion of the source, we then have a boosting factor $\delta = \Gamma^{-1}(1 - \beta\cos\phi)$, where ϕ (which we assume to be ~40) is the angle between the velocity vector and the line of sight, $\beta = v/c$ (assumed to be ~0.5) with c the speed of light, and $\Gamma = (1-\beta^2)^{1/2}$ represents the Lorentz factor.

This formalism allows us to calculate the magnetic field B and the inverse Compton scattered flux density $S_{\rm SSC}$ as a function of the energy of the X-ray photons $E_{\rm keV}$ (as given in Marscher 1983). The magnetic field strength is then defined as $B \propto \theta^4 \nu_m^5 S_m^{-2}$. Finally, the inverse Compton scattered flux is produced by scattering of the same electron population, and is defined as

$$S_{\rm SSC} \propto \ln(\nu_2/\nu_m)\theta^{-2(2\alpha+3)}\nu_m^{-(3\alpha+5)}S_m^{2(\alpha+2)}E_{\rm keV}^{-\alpha}, \quad (6)$$

where ν_2 is the upper synchrotron cutoff frequency. As explained above, a Lorentz factor of the order of 10^3 is required, for which ν_2 lies within the NIR bands. Most of the NIR spectrum can therefore be explained by synchrotron emission, whereas the inverse Compton emission is responsible for the X-ray spectrum (Markoff et al. 2001; Yuan et al. 2003; Eckart et al. 2004).

For the present study, we did not have simultaneous X-ray light curves at our disposal. However, as a further modeling constraint the SSC formalism has been applied, taking care that the derived X-ray values are consistent with literature data.

8.2. Source Components in Adiabatic Expansion

In the context of non-simultaneous flare emission, most of the observational evidence to date (e.g., Eckart et al. 2006b, 2008b; Yusef-Zadeh et al. 2006, 2009; Marrone et al. 2008) points toward the existence of a time delay of the order of 1–2 hr between the observed sub-mm flares and the prior events observed at shorter wavelengths (either X-ray or IR; see Marrone et al. 2008). There has been some discussion about whether or not these bursts of activity at different wavelengths have any relation. If the NIR/X-ray and radio/sub-mm events are unrelated, one should be able to see a comparable number of radio/sub-mm flares before and after the NIR/X-ray. Since this is not happening, it is therefore safe to assume that these energetic events are part of a common physical process taking place in Sgr A*.

In what follows we will introduce the basics of the adiabatic expansion model that has been applied to the synchrotron components described in Section 8.1. For full details of the adiabatic expansion formalism, the reader is referred to Eckart et al. (2008b) and references therein.

van der Laan (1966) was the first author to present a quantitative description of a model including initially thick synchrotron components that expand over time until they become optically thin at longer wavelengths. In our model the starting point is a compact, uniform spherical blob of radius R. This blob is composed of relativistic electrons and is characterized by an isotropic velocity distribution and a power-law energy distribution $n(E) \propto E^{-p}$. Initially, the assumption is such that the blob is optically thick at all frequencies. As it expands, the constant magnetic field, the energy of the relativistic particles, and their density change as R^{-2}, R^{-1}, and R^{-3}, respectively (van der Laan 1966).

The cutoff frequency is defined as ν_0, and R_0, S_0, and τ_0 represent the size, flux density, and optical depth of the blob. The optical depth and flux density are defined as

$$\tau = \tau_0 \left(\frac{\nu}{\nu_0}\right)^{-(p+4)/2} \left(\frac{R}{R_0}\right)^{-(2p+3)} \quad (7)$$

and

$$S_\nu = S_0 \left(\frac{\nu}{\nu_0}\right)^{5/2} \left(\frac{R}{R_0}\right)^3 \frac{1-e^{-\tau}}{1-e^{-\tau_0}} \quad (8)$$

in order to combine the adiabatic expansion model with the SSC formalism. τ_0 is defined as the optical depth corresponding to the frequency at which the flux density is a maximum (van der Laan 1966). Lastly, the dependence of the radius with time, $R(t)$, has been modeled linearly with a constant expansion speed $v_{\rm exp}$.

In summary, the present model is an attempt to describe the observed data by explaining the NIR luminosity with the optically thin, and the sub-mm luminosity with the optically thick regimes of the synchrotron emission.

8.3. Modeling the Flare Emission

Coordinated observations at NIR (VLT and Subaru) and sub-mm (APEX) wavelengths were possible during several nights of the observing run: 2008 May 27, 28, 29, 30, and 2008 June 3. Due to poor weather conditions, on May 28 the VLT NIR coverage was very short (about 1 hr) and took place in the middle of the sub-mm observations. Also, on the same night, the NIR Subaru data started when the sub-mm light curve finished. These aspects prevent us from providing a convincing simultaneous fit of the light curves. On May 29, we only have the Subaru and APEX data, which do not have a good time overlap. On May 30, the sub-mm light curve also has a poor time coverage, and is not adequate for a proper modeling.

For the other two light curves (May 27 and June 3; see Figure 2), we end up with light curves which are suitable for a simultaneous fitting. The Subaru data have not been used for the modeling because of the lack of time overlap between the facilities. Their main use in the present paper was to improve the statistics in Section 7.

The May 27 light curve presents mild VLT-NIR (*Ks*-band) variability with well-defined peaks. A strong sub-mm decay of more than 1.5 Jy is also measured, indicating that we missed at least the first half of the flare. This light curve is explained, in the context of our model, with three flare events (see Figure 10), which do not include the Subaru data. In the sub-mm domain the emission is dominated by a broad flare, a combination of the three individual events observed in the NIR.

In the data set corresponding to June 3, violent variability is detected in the NIR (L' and *Ks* bands) with, under the assumption of the adiabatic expansion model, a significant counterpart in the sub-mm domain. This flare has been extensively studied and modeled by Eckart et al. (2008b); therefore, here we will only discuss the values to compare them with the present modeling. In that case four different events are necessary to account for the measured NIR variability, while in the sub-mm domain the components blend in a single flare.

To account for the slow variability of Sgr A* (scale of days; see, e.g., Zhao et al. 2001; Meyer et al. 2008), a constant value of 3.2 Jy has been subtracted from the May 27 light curve. This value is in good agreement with the offset of 3.0 ± 0.5 Jy estimated statistically by Eckart et al. (2008b).

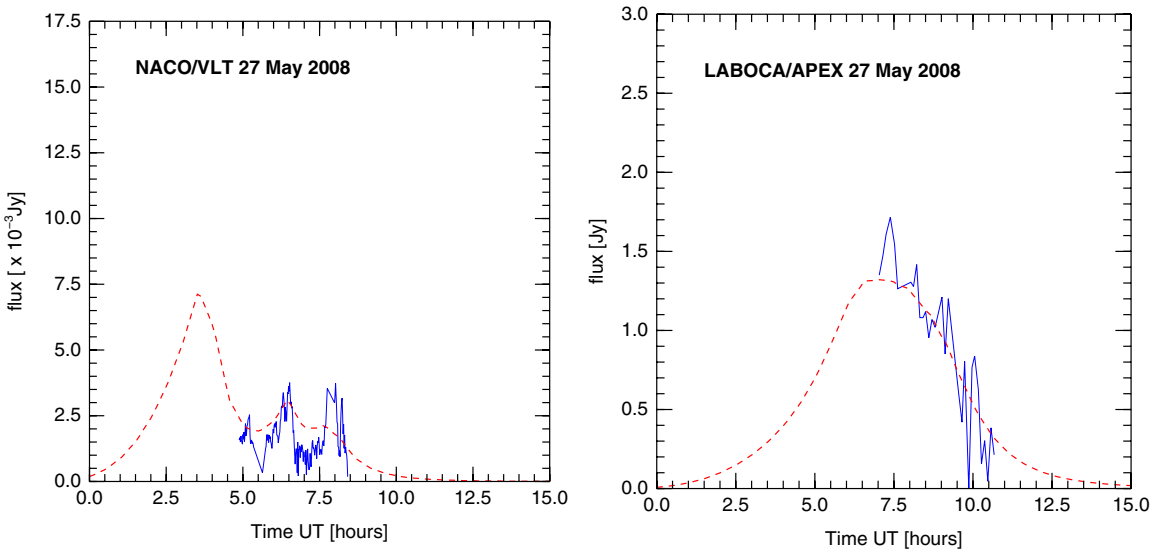

Figure 10. Left: the blue solid line represents the Sgr A* NIR light curve for 2008 May 27. The red dashed line represents the proposed models described in Table 6. Right: same but for the sub-mm emission.

(A color version of this figure is available in the online journal.)

Table 6
Parameters of the SSC Model

Model Comp.[a]	γ_1[b]	γ_2[c]	S_0[d]	α_{synch}[e]	R_0[f]	ν_0[g]	B[h]	S_{NIR}[i]	S_{NIR}[j]	S_{X-ray}[k]
Label			(Jy)		(R_S)	(GHz)	(G)	sync (mJy) @2.2 μm	SSC (mJy) @2.2 μm	SSC (μJy) @4 keV
1σ			1.8	0.10	0.17	290	15	0.7	1.0	0.4
2008 May 27 I	10.0	3200	5.5	1.48	0.95	1300	85.0	5.6	0.0	0.02
2008 May 27 II	10.0	3500	1.4	1.45	0.55	1150	79.0	1.4	0.0	0.12
2008 May 27 III	10.0	3500	1.4	1.30	0.95	700	61.6	1.5	0.4	0.004

Notes.
[a] Flare label.
[b] Minimum electron Lorentz factor.
[c] Maximum electron Lorentz factor.
[d] Flux density at ν_0.
[e] Spectral index.
[f] Size of the expanding uniform blob of relativistic electrons in Schwarzschild radii.
[g] Turnover frequency.
[h] Magnetic field.
[i] NIR synchrotron flux density.
[j] NIR synchrotron self-Compton flux density.
[k] X-ray synchrotron self-Compton flux density.

8.3.1. Modeling Results

We have constructed a plausible model for the May 27 light curves using the observational data and three adiabatically expanding source components in agreement with an SSC formalism (Figure 10). We note that one strong assumption of the modeling is that there is a first NIR component for which we have no observations. Before adding this component, several models with only two components were tested without success. Large variations in the expansion velocity, spectral index, or cutoff frequency did not give any result that was similar to the observed data. A model in which NIR and sub-mm flares are simultaneous is rejected because the observed light-curve structures do not fit. This is why we finally decide to include this extra component. So what we do here is present a model which is a fair representation of the observations. Table 6 accounts for the most relevant parameters of our best SSC model. There the order of magnitude of γ_2 is consistent with the ones defined in Section 8.1. The spectral index for the three events is consistent with 1.4 ± 0.1, and the initial size of the source components ranges from 0.55 to 0.95 ± 0.15 Schwarzschild radii. Their flux densities are of the order of a few Jy, and the turnover frequencies are between 0.7 and 1.3 THz. All these values compare well with the ones resulting from fitting the flare on 2008 June 3 (see Eckart et al. 2008b). The X-ray fluxes are less than about 150 nJy, which is close to the mean of what has been observed in X-ray flares. With the given sub-mm fluxes, cutoff frequency, and spectral indices, the brightest component gives an 8.6 μm flux which is within 1σ of the upper limit obtained at that wavelength by Schödel et al. (2007).

We obtain magnetic fields whose values go from about 61 to 85 G, which are comparable with those derived from early observations. The sum of the synchrotron and SSC NIR flux

is roughly consistent with the observed values, within the uncertainties. These SSC results constrain our model and are consistent with a slow adiabatic expansion velocity of 0.18% of c.

8.4. Implications of the Modeling Results

The adiabatic expansion modeling is consistent with a time lag of 3.0 ± 0.5 hr between the VLT and APEX light curves, which is about double the previous results obtained from our team (see Eckart et al. 2008a, 2008b; Kunneriath et al. 2010) and other authors (e.g., Yusef-Zadeh et al. 2009, and references therein). The results from the present campaign, along with other coordinated observing campaigns that include sub-mm monitoring of Sgr A* (Eckart et al. 2006b, 2008b; Yusef-Zadeh et al. 2006, 2009; Marrone et al. 2008), suggest that non-radiative cooling processes, such as adiabatic expansion, are needed. However, the adiabatic cooling model results in very low expansion speeds. Based on the model of millimeter radio flares, Yusef-Zadeh et al. (2008) obtained expansion velocities in the range $0.003c \lesssim v_{\rm exp} \lesssim 0.1c$. Our value of $0.0018c$ is at the lower end of this interval. All of these velocities are slow compared to the expected relativistic sound speed and the orbital velocity in the vicinity of an SMBH. These low expansion velocities suggest that the expanding gas cannot escape from Sgr A*, or that it has a large bulk motion superimposed on the expansion (see for instance Marrone et al. 2008; Yusef-Zadeh et al. 2009). This implies that the adiabatically expanding source components have a bulk motion larger than $v_{\rm exp}$. Alternatively, the expanding material may be contributing to a corona or disk close to Sgr A*. Differential rotation within the accretion disk may also account for the low expansion velocities.

9. SUMMARY

This paper presents a global and consistent view of the mechanisms dominating the inner parsecs of the GC, including the characterization of the variability of its black hole. We present the results of the coordinated campaign between APEX and VLT to obtain simultaneous sub-mm/NIR measurements of Sgr A*, the counterpart associated with an SMBH in the center of the Milky Way. These data, along with NIR light curves obtained with the Subaru telescope, have been used to characterize the variability of Sgr A*. Also, as part of the APEX observations, we obtained a high S/N sub-mm map of the 37 × 34 central pc^2 of our galaxy. With this map we have derived the masses of the most important molecular clouds and the CND. In addition to this, JCMT sub-mm archive maps have also been used.

The most important results are summarized below.

1. The structure of the most relevant molecular clouds corresponds well to the ones detected by previous sub-mm studies. They are also consistent with the previously published atomic emission and molecular transition maps. The 870 μm flux of these clouds and the CND vary from about 35 to 320 Jy, and their masses from about 5 to 47 × 10^5 $M_\odot$.
2. The temperature distribution derived from the 450 μm and 850 μm maps suggests the presence of quite cold and homogeneous dust in the molecular clouds, with temperatures between 10 and 20 K for most cases. In some regions, including the CND, the temperature is apparently $\leqslant$10 K. These low values are probably unphysical; they are rather an indication for the presence of non-thermal emission mechanisms.
3. The spectral index map shows that for the 20 and 50 km s^{-1} clouds the thermal dust emission is responsible for the measured fluxes. However, especially for the CND and surroundings, the spectral indices decrease toward Sgr A* and cover a range between about 1 and −0.6. These values are mostly explained as a combination of dust, synchrotron, and free–free emission in different ratios. The presence of non-thermal emission also accounts for the low temperatures derived in these areas, indicating that the fluxes cannot be used to derive temperatures straight away. We argue that a significant portion of non-thermal 350 GHz radio emission may also be associated with compact pulsar/neutron stars and their winds.
4. From our NIR light curves, we find that the typical activity peak is at 14.1 ± 5.5 mJy, and that the median activity length is 5.3 ± 0.7 hr. For the case of the sub-mm light curves, the typical peak value is 4.3 ± 0.4 Jy.
5. We have proposed a classification scheme for the NIR flares, using four different types. There the observed light curves are defined with a combination of individual short events (i.e., hot spots) and an underlying transient small disk. Strongly variable episodes with an underlying main flare represent one-quarter of the classified flares, whereas short individual events, either clustered or sparse, are in the majority.
6. For the May 27 NIR/sub-mm flare, our model results in a time lag between both wavelengths of about 3.0 ± 0.5 hr. We argue that this delay of the sub-mm with respect to the NIR light curve is due to the adiabatic expansion of the synchrotron source components which become optically thin in the sub-mm domain. The expansion velocity is somewhat slow, about 540 km s^{-1} (0.18% of the speed of light). In any case, our results for the light-curve modeling are consistent with an SSC formalism. For one of the light curves we used four components, whereas the other needed three. These components are clearly distinguishable in the NIR domain, but they are broader and blend with each other in the sub-mm.
7. We have shown that the combination APEX–VLT is ideal for obtaining long, simultaneous light curves in the NIR and sub-mm domains. Comparatively, the Subaru data are not sufficiently well synchronized with APEX, but this could be remedied in the future with observations by the Submillimeter Array.

The authors thank the anonymous referee for the insightful comments and constructive review of the manuscript. We are grateful to the ESO Sequitor and Paranal staff, and especially to the members of the APEX, NAOS/CONICA, and VLT teams. The observations were made possible through an especial effort by the APEX/ONSALA staff to have the LABOCA bolometer ready for triggering. This research used the facilities of the Canadian Astronomy Data Centre operated by the National Research Council of Canada with the support of the Canadian Space Agency. The James Clerk Maxwell Telescope is operated by the Joint Astronomy Centre on behalf of the Science and Technology Facilities Council of the United Kingdom, the Netherlands Organisation for Scientific Research, and the National Research Council of Canada. Macarena García-Marín is supported by the German federal department for education and research (BMBF) under the project numbers 50OS0502 and 50OS0801. M. Zamaninasab and D. Kunneriath were members of the International Max Planck Research School (IMPRS) for Astronomy

and Astrophysics at the MPIfR and the Universities of Bonn and Cologne. N. Sabha is a member of the Bonn Cologne Graduate School for Physics and Astronomy. R. Schödel acknowledges support by the Ramón y Cajal program by the Ministerio de Ciencia e Innovación for the government of Spain. This paper uses the plotting package `jmaplot`, developed by Jesús Maíz-Apellániz. http://dae45.iaa.csic.es:8080/∼jmaiz/software.

REFERENCES

Anantharamaiah, K. R., Pedlar, A., Ekers, R. D., & Goss, W. M. 1991, MNRAS, 249, 262
Bremer, M., et al. 2011, A&A, in press
Burton, M., & Allen, D. 1992, Proc. Astron. Soc. Aust., 10, 55
Christopher, M. H., Scoville, N. Z., Stolovy, S. R., & Yun, M. S. 2005, ApJ, 622, 346
Davidson, J. A., Werner, M. W., Wu, X., Lester, D. F., Harvey, P. M., Joy, M., & Morris, M. 1992, ApJ, 387, 189
Dent, W. R. F., Matthews, H. E., Wade, R., & Duncan, W. D. 1993, ApJ, 410, 650
Diolaiti, E., Bendinelli, O., Bonaccini, D., Close, L., Currie, D., & Parmeggiani, G. 2000, A&AS, 147, 335
Do, T., Ghez, A. M., Morris, M. R., Yelda, S., Meyer, L., Lu, J. R., Hornstein, S. D., & Matthews, K. 2009, ApJ, 691, 1021
Dodds-Eden, K., et al. 2009, ApJ, 698, 676
Dodds-Eden, K., et al. 2011, ApJ, 728, 37
Dubner, G., Giacani, E., & Decourchelle, A. 2008, A&A, 487, 1033
Eckart, A., & Genzel, R. 1996, Nature, 383, 415
Eckart, A., & Genzel, R. 1997, MNRAS, 284, 576
Eckart, A., Genzel, R., Ott, T., & Schödel, R. 2002, MNRAS, 331, 917
Eckart, A., Schödel, R., Meyer, L., Trippe, S., Ott, T., & Genzel, R. 2006a, A&A, 455, 1
Eckart, A., et al. 2004, A&A, 427, 1
Eckart, A., et al. 2006b, A&A, 450, 535
Eckart, A., et al. 2008a, A&A, 479, 625
Eckart, A., et al. 2008b, A&A, 492, 337
Eisenhauer, F., Schödel, R., Genzel, R., Ott, T., Tecza, M., Abuter, R., Eckart, A., & Alexander, T. 2003, ApJ, 597, L121
Ekers, R. D., van Gorkom, J. H., Schwarz, U. J., & Goss, W. M. 1983, A&A, 122, 143
Falcke, H., Markoff, S., & Bower, G. C. 2009, A&A, 496, 77
Gatley, I., Jones, T. J., Hyland, A. R., Wade, R., Geballe, T. R., & Krisciunas, K. 1986, MNRAS, 222, 299
Genzel, R., Schödel, R., Ott, T., Eckart, A., Alexander, T., Lacombe, F., Rouan, D., & Aschenbach, B. 2003, Nature, 425, 934
Genzel, R., Watson, D. M., Townes, C. H., Dinerstein, H. L., Hollenbach, D., Lester, D. F., Werner, M., & Storey, J. W. V. 1984, ApJ, 276, 551
Ghez, A. M., Morris, M., Becklin, E. E., Tanner, A., & Kremenek, T. 2000, Nature, 407, 349
Ghez, A. M., Salim, S., Hornstein, S. D., Tanner, A., Lu, J. R., Morris, M., Becklin, E. E., & Duchêne, G. 2005, ApJ, 620, 744
Ghez, A. M., et al. 2008, ApJ, 689, 1044
Gillessen, S., Eisenhauer, F., Trippe, S., Alexander, T., Genzel, R., Martins, F., & Ott, T. 2009, ApJ, 692, 1075
Gillessen, S., et al. 2006, ApJ, 640, L163
Gould, R. J. 1979, A&A, 76, 306
Guesten, R., Genzel, R., Wright, M. C. H., Jaffe, D. T., Stutzki, J., & Harris, A. I. 1987, ApJ, 318, 124
Guesten, R., Walmsley, C. M., & Pauls, T. 1981, A&A, 103, 197
Harris, A. I., Jaffe, D. T., Silber, M., & Genzel, R. 1985, ApJ, 294, L93
Herrnstein, R. M. 2003, PhD thesis, Harvard-Smithsonian Center for Astrophysics
Herrnstein, R. M., & Ho, P. T. P. 2002, ApJ, 579, L83
Herrnstein, R. M., & Ho, P. T. P. 2005, ApJ, 620, 287
Hildebrand, R. H. 1983, QJRAS, 24, 267
Holland, W. S., et al. 1999, MNRAS, 303, 659
Hornstein, S. D., Matthews, K., Ghez, A. M., Lu, J. R., Morris, M., Becklin, E. E., Rafelski, M., & Baganoff, F. K. 2007, ApJ, 667, 900
Iye, M., et al. 2004, PASJ, 56, 381
Jackson, J. M., Heyer, M. H., Paglione, T. A. D., & Bolatto, A. D. 1996, ApJ, 456, L91
Jenness, T., & Lightfoot, J. F. 1998, in ASP Conf. Ser. 145, Astronomical Data Analysis Software and Systems VII, ed. R. Albrecht, R. N. Hook, & H. A. Bushouse (San Francisco, CA: ASP), 216
Kramer, C., Richer, J., Mookerjea, B., Alves, J., & Lada, C. 2003, A&A, 399, 1073
Kunneriath, D., et al. 2010, A&A, 517, A46
Latvakoski, H. M., Stacey, G. J., Gull, G. E., & Hayward, T. L. 1999, ApJ, 511, 761
Lenzen, R., et al. 2003, Proc. SPIE, 4841, 944
Lis, D. C., & Carlstrom, J. E. 1994, ApJ, 424, 189
Lis, D. C., Carlstrom, J. E., & Keene, J. 1991, ApJ, 380, 429
Lu, J. R., Ghez, A. M., Hornstein, S. D., Morris, M. R., Becklin, E. E., & Matthews, K. 2009, ApJ, 690, 1463
Lucy, L. B. 1974, AJ, 79, 745
Maeda, Y., et al. 2002, ApJ, 570, 671
Maitra, D., Markoff, S., & Falcke, H. 2009, A&A, 508, L13
Markoff, S., Falcke, H., Yuan, F., & Biermann, P. L. 2001, A&A, 379, L13
Marrone, D. P., et al. 2008, ApJ, 682, 373
Marscher, A. P. 1983, ApJ, 264, 296
Mauerhan, J. C., Morris, M., Walter, F., & Baganoff, F. K. 2005, ApJ, 623, L25
Meyer, L., Do, T., Ghez, A., Morris, M. R., Witzel, G., Eckart, A., Bélanger, G., & Schödel, R. 2008, ApJ, 688, L17
Meyer, L., Do, T., Ghez, A., Morris, M. R., Yelda, S., Schödel, R., & Eckart, A. 2009, ApJ, 694, L87
Meyer, L., Eckart, A., Schödel, R., Duschl, W. J., Mužić, K., Dovčiak, M., & Karas, V. 2006a, A&A, 460, 15
Meyer, L., Schödel, R., Eckart, A., Karas, V., Dovčiak, M., & Duschl, W. J. 2006b, A&A, 458, L25
Mezger, P. G., Zylka, R., Salter, C. J., Wink, J. E., Chini, R., Kreysa, E., & Tuffs, R. 1989, A&A, 209, 337
Migliari, S., et al. 2007, ApJ, 671, 706
Montero-Castaño, M., Herrnstein, R. M., & Ho, P. T. P. 2009, ApJ, 695, 1477
Muno, M. P., Baganoff, F. K., Brandt, W. N., Morris, M. R., & Starck, J. 2008, ApJ, 673, 251
Nishiyama, S., Tamura, M., Hatano, H., Nagata, T., Kudo, T., Ishii, M., Schödel, R., & Eckart, A. 2009a, ApJ, 702, L56
Nishiyama, S., et al. 2009b, ApJ, 690, 1648
Oka, T., Hasegawa, T., Handa, T., Hayashi, M., & Sakamoto, S. 1996, ApJ, 460, 334
Okumura, S. K., Ishiguro, M., Fomalont, E. B., Hasegawa, T., Kasuga, T., Morita, K.-I., Kawabe, R., & Kobayashi, H. 1991, ApJ, 378, 127
Pestalozzi, M., Torkelsson, U., Hobbs, G., & López-Sánchez, Á. R. 2009, A&A, 506, L21
Pierce-Price, D., et al. 2000, ApJ, 545, L121
Reid, M. J. 1993, ARA&A, 31, 345
Richardson, W. H. 1972, J. Opt. Soc. Am., 62, 55
Rousset, G., et al. 2003, Proc. SPIE, 4839, 140
Sabha, N., et al. 2010, A&A, 512, A2
Schnee, S., & Goodman, A. 2005, ApJ, 624, 254
Schödel, R., Eckart, A., Mužić, K., Meyer, L., Viehmann, T., & Bower, G. C. 2007, A&A, 462, L1
Schödel, R., et al. 2002, Nature, 419, 694
Siringo, G., et al. 2009, A&A, 497, 945
Takami, H., et al. 2004, Proc. SPIE, 5490, 837
Tamura, M., Fukagawa, M., Murakawa, K., Suto, H., Itoh, Y., & Doi, Y. 2003, Proc. SPIE, 4843, 190
Tsuboi, M., Handa, T., & Ukita, N. 1999, ApJS, 120, 1
van der Laan, H. 1966, Nature, 211, 1131
Wright, M. C. H., Coil, A. L., McGary, R. S., Ho, P. T. P., & Harris, A. I. 2001, ApJ, 551, 254
Yuan, F., Quataert, E., & Narayan, R. 2003, ApJ, 598, 301
Yusef-Zadeh, F., Hewitt, J. W., & Cotton, W. 2004, ApJS, 155, 421
Yusef-Zadeh, F., & Morris, M. 1987a, AJ, 94, 1178
Yusef-Zadeh, F., & Morris, M. 1987b, ApJ, 320, 545
Yusef-Zadeh, F., & Morris, M. 1987c, ApJ, 322, 721
Yusef-Zadeh, F., Morris, M., Slee, O. B., & Nelson, G. J. 1986, ApJ, 310, 689
Yusef-Zadeh, F., Stolovy, S. R., Burton, M., Wardle, M., & Ashley, M. C. B. 2001, ApJ, 560, 749
Yusef-Zadeh, F., Wardle, M., Heinke, C., Dowell, C. D., Roberts, D., Baganoff, F. K., & Cotton, W. 2008, ApJ, 682, 361
Yusef-Zadeh, F., et al. 2006, ApJ, 644, 198
Yusef-Zadeh, F., et al. 2009, ApJ, 706, 348
Zamaninasab, M., et al. 2010, A&A, 510, A3
Zhao, J., Bower, G. C., & Goss, W. M. 2001, ApJ, 547, L29
Zylka, R., Mezger, P. G., & Wink, J. E. 1990, A&A, 234, 133